Front. Optoelectron. 2014, 7(2): 220–242
DOI 10.1007/s12200-014-0398-2

RESEARCH ARTICLE

Application of broadband terahertz spectroscopy in semiconductor nonlinear dynamics

I-Chen HO (✉)[1], Xi-Cheng ZHANG (✉)[2,3]

1 Rensselaer Polytechnic Institute, Troy, NY 12180-3590, USA
2 The Institute of Optics, University of Rochester, Rochester, NY 14627-0186, USA
3 Wuhan National Laboratory for Optoelectronics, Huazhong University of Science and Technology, Wuhan 430074, China

Abstract Semiconductor nonlinearity in the range of terahertz (THz) frequency has been attracting considerable attention due to the recent development of high-power semiconductor-based nanodevices. However, the underlying physics concerning carrier dynamics in the presence of high-field THz transients is still obscure. This paper introduces an ultrafast, time-resolved THz pump/THz probe approach to study semiconductor properties in a nonlinear regime. The carrier dynamics regarding two mechanisms, intervalley scattering and impact ionization, was observed for doped InAs on a sub-picosecond time scale. In addition, polaron modulation driven by intense THz pulses was experimentally and theoretically investigated. The observed polaron dynamics verifies the interaction between energetic electrons and a phonon field. In contrast to previous work which reported optical phonon responses, acoustic phonon modulations were addressed in this study. A further understanding of the intense field interacting with solid materials will accelerate the development of semiconductor devices.

This paper can be divided into 4 sections. Section 1 starts with the design and performance of a table-top THz spectrometer, which has the advantages of ultra-broad bandwidth (one order higher bandwidth compared to a conventional ZnTe sensor) and high electric field strength (>100 kV/cm). Unlike the conventional THz time-domain spectroscopy, the spectrometer integrated a novel THz air-biased-coherent-detection (THz-ABCD) technique and utilized gases as THz emitters and sensors. In comparison with commonly used electro-optic (EO) crystals or photoconductive (PC) dipole antennas, the gases have the benefits of no phonon absorption as existing in EO crystals and no carrier life time limitation as observed in PC dipole antennas. In Section 2, the newly development THz-ABCD spectrometer with a strong THz field strength capability provides a platform for various research topics especially on the nonlinear carrier dynamics of semiconductors. Two mechanisms, electron intervalley scattering and impact ionization of InAs crystals, were observed under the excitation of intense THz field on a sub-picosecond time scale. These two competing mechanisms were demonstrated by changing the impurity doping type of the semiconductors and varying the strength of the THz field.

Another investigation of nonlinear carrier dynamics in Section 3 was the observation of coherent polaron oscillation in n-doped semiconductors excited by intense THz pulses. Through modulations of surface reflection with a THz pump/THz probe technique, this work experimentally verifies the interaction between energetic electrons and a phonon field, which has been theoretically predicted by previous publications, and shows that this interaction applies for the acoustic phonon modes. Usually, two transverse acoustic (2TA) phonon responses are inactive in infrared measurement, while they are detectable in second-order Raman spectroscopy. The study of polaron dynamics, with nonlinear THz spectroscopy (in the far-infrared range), provides a unique method to diagnose the overtones of 2TA phonon responses of semiconductors, and therefore incorporates the abilities of both infrared and Raman spectroscopy. Finally, some conclusions were presented in Section 4. In a word, this work presents a new milestone in wave-matter interaction and seeks to benefit the industrial applications in high power, small scale devices.

Received December 5, 2013; accepted February 18, 2014

E-mail: karenhothz@gmail.com, xi-cheng.zhang@rochester.edu

Keywords terahertz (THz), nonlinear, spectroscopy, broadband, semiconductor

1 Broadband terahertz spectroscopy (air-biased-coherent-detection)

1.1 Time-domain spectroscopy: terahertz wave air photonics

Generation and detection of terahertz (THz) waves with selected gases is a technology that has been developed during the past decade [1–7]. Figure 1 illustrates a typical air-plasma-based THz wave generation and detection setup.

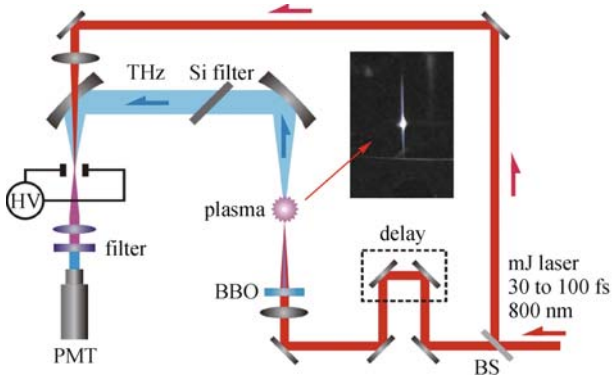

Fig. 1 Schematic illustration of broadband THz wave generation and detection. BS, beam splitter; BBO, beta barium borate; HV, high voltage bias; PMT, photomultiplier tube

THz wave air photonics, using selected gases as the THz wave emitter and sensor, brings the advantages of intense electric field and broad spectral bandwidth. Furthermore, compared to conventional emitters and detectors, the gases overcome the bandwidth limitation due to the phonon absorption in electro-optic (EO) crystals or the carrier lifetime in photoconductive (PC) antennas. A useful bandwidth continuously covering from 0.5 to 35 THz, together with intense peak electric field in time domain has been achieved with a reflective THz air-biased-coherent-detection (R-THz-ABCD) spectrometer [7], as shown in Fig. 2.

Therefore, a terahertz time-domain spectroscopy (THz-TDS) system, integrated with the THz wave air photonics, not only fulfills the broad bandwidth and intense electric field requirements, but also enables the study of transient carrier dynamics. A further advance of THz pump-probe technique for studying semiconductor nonlinearity will be introduced in Sections 2 and 3.

1.2 Experimental setup: air-biased-coherent-detection

The design, performance, and evaluation of a reflective terahertz time-domain spectroscopy (R-THz-TDS), using air materials as THz wave emitter and sensor, together with air-biased-coherent-detection (ABCD) technique is reported. The uniqueness and advantage of this spectrometer are comprehensively compared with traditional THz-TDS and Fourier transform infrared (FTIR) spectroscopy. The study of the THz-ABCD spectrometer provides a useful tool for investigating semiconductor nonlinear responses in Sections 2 and 3.

1.2.1 Background review

Over the last two decades, THz-TDS has undergone extensive developments within various regions: THz imaging, bio-sensing, materials testing, as well as carrier dynamics studying [8–12]. However, the high-power and

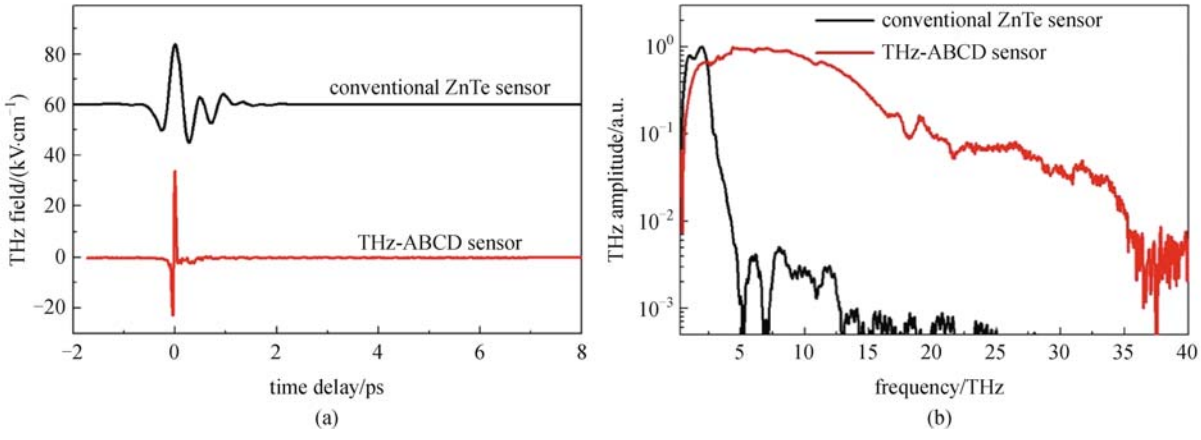

Fig. 2 (a) Measured time-domain waveforms with a conventional ZnTe sensor (black curve) and with a THz-ABCD sensor (red curve). The air plasma is utilized as an emitter in both measurements; (b) corresponding spectra obtained through discrete Fourier transform of the THz waveforms. The frequency range from 0.5 to 35 THz in THz-ABCD shows one order of bandwidth improvement in comparison with a conventional ZnTe sensor

broad-bandwidth THz field is still much less developed. Although several groups have developed a strong THz source via $LiNbO_3$ crystal in a table top system [13,14], the bandwidth is limited below 3 THz. On the other hand, a wideband THz response (up to 15 THz) using organic, EO polymer emitter-sensor pairs were recently reported [15]. The polymer material with EO coefficient > 300 pm/V provides strong THz generation (several kV/cm) and sensitive THz detection. However, the performance of the polymer decreases with time.

Intense THz waves generated from laser-induced plasma in gaseous media provide more promising bandwidth due to no phonon absorption as in EO crystals or no carrier lifetime limitation as in photo-conductors [1–4,16,17]. The Center for THz Research at Rensselaer applies dry air (or selected gases) as the emitter and detection medium [5,18] and furthermore integrates the THz-ABCD technique [6]. Gap-free emission and detection with higher signal-to-noise ratio (SNR > 1000), compared to other methods, have been obtained. The useable bandwidth is only limited by laser pulse duration.

1.2.2 Reflection spectroscopy

The reflection spectroscopy is usually performed in opaque materials. Compared to the commonly used transmission spectroscopy, the reflection geometry comes with the added difficulty of great sensitivity of the incident angle and the sample position. A normal incident angle with a long focal length might reduce the incident angle issue. However, the precise determination of the sample position is difficult, but essential, to properly determine the phase spectra. Several experimental methods to correct the phase errors have been proposed [19–26].

Rønne et al. made use of specific sample properties to avoid the position error between the sample and the reference [19]; Khazan et al. extracted the complex function from the s- and p-polarized THz waves reflected from the sample [22,23]. These methods are demonstrated in particular cases. On the other hand, Nashima et al. attached a slab in front of the sample surface, which comes with a problem of the contact between two samples [24]. Regarding the temporal stability of the whole setup,

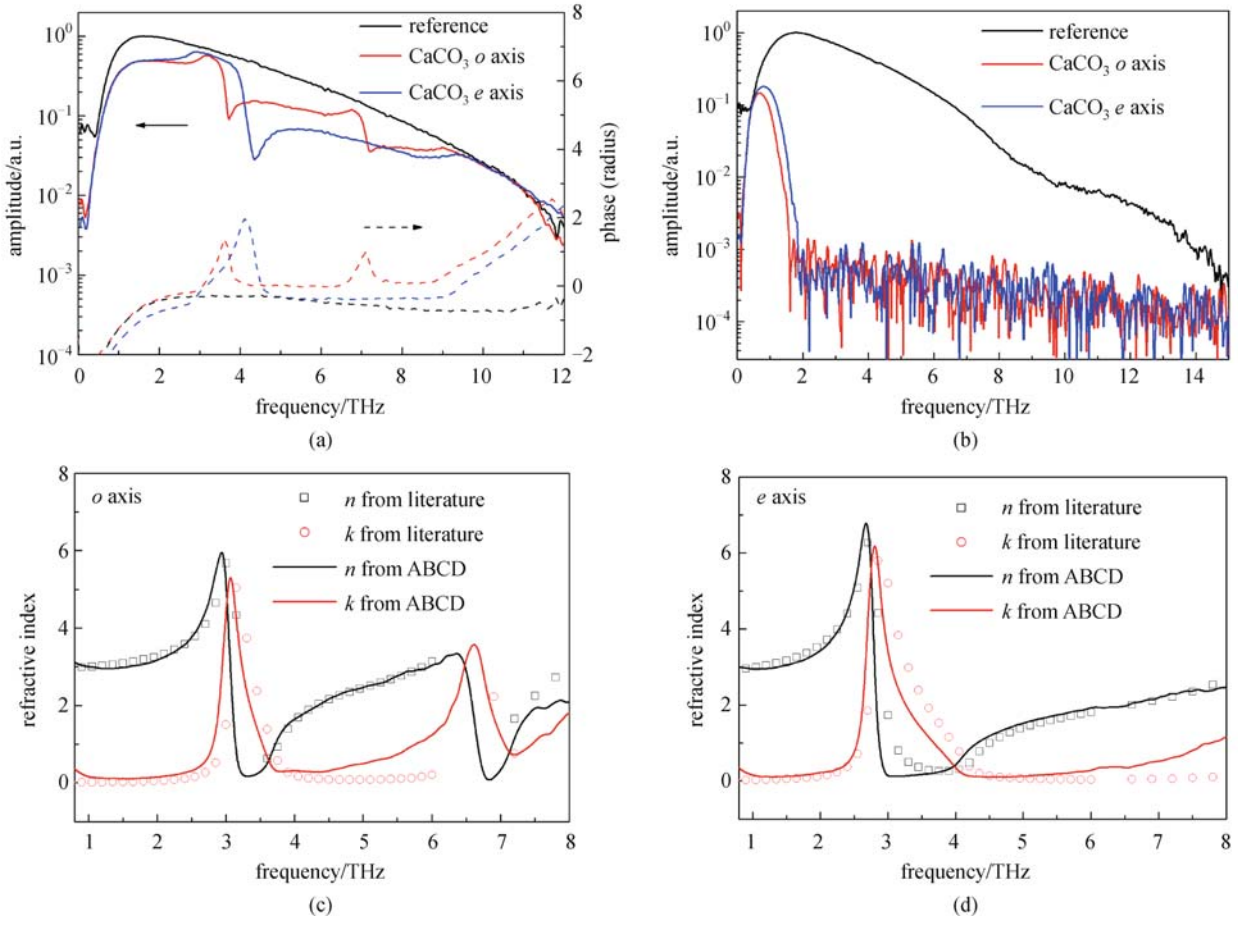

Fig. 3 (a) Measured reflection spectra of a $CaCO_3$ crystal and the reference (solid lines) as well as measured phase responses (dashed lines); (b) measured transmission spectra of the same crystal; (c) refractive indices (n and k) of o axis from 0.8 to 8 THz according to (a); (d) refractive indices (n and k) of e axis from 0.8 to 8 THz according to (a)

including the beam-pointing stability of the laser source and the repeatability of the delay stage, the limit factor results not only from precise positioning of the sample but the temporal stability. To achieve our best fits, the relative positions were theoretically adjusted by typically ±5 μm. This is similar to the problem solved in transmission THz-TDS, involving the precision of the sample thickness [25].

Even though the reflection spectroscopy has the intrinsic difficulty, regarding the high absorption in bulk samples, the reflection module provides a better spectral range than transmission geometry. Figure 3 shows the spectra of a $CaCO_3$ sample measured with both modules. The thickness of an X-cut $CaCO_3$ crystal is 2.8 mm and its optical quality area is 15 mm × 18 mm without coating. In the reflection measurement of Fig. 3(a), it clearly shows the different optical properties between *e* and *o* axes when the sample is rotated with respect to the pre-dominated p-polarization of the THz field. The dashed curves show the phase responses corresponding to the spectra. Figure 3(b) is the transmission spectra of the same crystal. No features can be resolved from these data due to the large absorption and the spectra above 1.8 THz are merged in the noise floor. According to Fig. 3(a), the phonon resonances at 3.06 and 6.61 THz of *o* axis are shown in Fig. 3(c) while one phonon resonance at 2.82 THz of *e* axis is shown in Fig. 3(d), which is in agreement with Ref. [27]. Here, the reflective indices (real part: *n* and imaginary part: *k*) based on Ref. [27] are re-plotted with scatters.

1.2.3 Mechanisms of terahertz waves generation and detection in air

THz wave air photonics is applied for THz wave's generation and detection, which is simply explained by a third order nonlinear optics process. Regarding the generation part, Cook and Hochstrasser [1], Bartel et al. [17], and Xu et al. [2] have experimentally demonstrated THz wave generation in air and initially treated it through perturbation as four-wave mixing (FWM). The THz field has the form:

$$E_{\mathrm{THz}}(t) \propto \chi^{(3)}_{\mathrm{eff}} E_{2\omega}(t) E^{*}_{\omega}(t) E^{*}_{\omega}(t) \cos(\varphi), \qquad (1)$$

where φ is the relative phase difference between the ω and 2ω beams, $\chi^{(3)}_{\mathrm{eff}}$ is the effective third-order susceptibility of air material, and E is the electric field component associated with the optical or the THz field. In the FWM model, the THz photon energy is given by the differential frequency between the sum frequency of the two photons from the fundamental pulses (ω) and the frequency of one photon from the second harmonic (SH) pulses (2ω). With a shorter pulse duration of the optical pump pulses, a larger differential frequency range is possible so that the THz pulse with a broader bandwidth is generated. Accordingly, a pulse with broader THz bandwidth is generated by shorter optical pulse duration. Later, Kim et al. [3] proposed a semi-classical picture to explain the THz wave generation.

Recently, Karpowicz and Zhang [4] applied a quantum mechanics model to provide a unique way to look at emitted THz waves. In this model, the THz generation process takes place in two steps. First, the atoms or molecules are asymmetrically ionized within a fraction of the optical pulses, resulting in a broadband THz transient. Second, the released electron wave packets interact with the surrounding medium, resulting in the loss of their coherent motion, which produces a lower-frequency echo with frequency components below the inverse of the scattering time.

In the detection part, Dai et al. [5] reported broadband THz detection via THz-field-induced second-harmonic (TFISH) generation in laser-induced plasma. In the reciprocal process of THz wave generation in air plasma, TFISH in third-order nonlinear process can be expressed as

$$E_{2\omega}(t) \propto \chi^{(3)} E_{\mathrm{THz}}(t) E^{*}_{\omega}(t) E^{*}_{\omega}(t). \qquad (2)$$

Again, shorter pulse duration of the optical probe pulse make a broader sensing bandwidth, which is the similar mechanism as with the THz generation.

1.2.4 Experimental design

The broadband R-THz-ABCD spectrometer is schematically shown in Fig. 4. A Ti-sapphire amplified laser (Spectra-Physics Hurricane) with a central wavelength of 800 nm, 85 fs (full width at half maximum, FWHM) pulse duration, 750 μJ pulse energy, and 1 kHz repetition rate is used as the optical source. The laser beam is separated into two beams by an optical beam splitter so that one beam with 75% energy passes through a motorized delay line and a 100 μm thick type-I beta barium borate (BBO) crystal, by which the 400 nm SH is generated. The fundamental (ω) and SH (2ω) beam are focused in dry nitrogen with a lens of 150 mm effective focal length. The pre-dominantly p-polarized THz emission from the laser-induced plasma is collimated and refocused by a pair of parabolic mirrors P1 (4" focal length) and P2 (6" focal length), and then reflected back by the sample surface located at the focal point of the parabolic mirror P2. The reflected beam is collimated again by P2. A high resistivity silicon beam splitter steers the backward THz beam by 90° to the detection part. The residual 25% optical energy is guided through the hole of the parabolic mirror P3 (2" focal length) as the probe beam.

Both THz and optical probe beams are focused between two needle-shaped electrodes with 1 mm distance. SH generation is induced through the nonlinear interaction of the probe field, the THz field, and the bias electric field, and its intensity is proportional to THz electrical field and local bias field strengths. A laser-synchronized alternating bias ±20 kV/cm at 500 Hz was applied by a high voltage

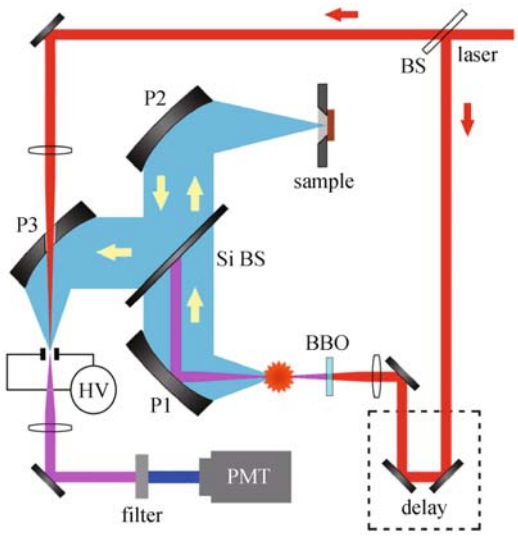

Fig. 4 Experimental setup. The THz beam is generated by mixing the fundamental and SH beams (after a type-I beta BBO crystal) at the air plasma point in front of parabolic mirror P1. A high resistivity silicon wafer acts as a beam splitter which blocks the residual 800 and 400 nm beams, but passes and reflects the THz beam. The sample position is located at the focal point of parabolic mirror P2. The THz beam is detected by measuring the coherent time-resolved SH signal induced by mixing the probe field, the THz field, and the alternating current (AC) bias electrical field at the focal point of P3

(HV) modulator. It introduces an alternating current (AC) external bias to the optical focus point between two needle-shaped electrodes, where a bias-field-induced SH pulse is generated to improve the dynamics range (DR) and ensure coherent detection [6]. The coherent field-induced SH generation is selected by several band pass filters and detected by a photomultiplier tube (PMT) (Hamamatsu H7732-10). Figure 5(a) is the time-domain waveform and Fig. 5(b) is the Fourier transform spectrum of Fig. 5(a). The DR in Fig. 5(a) is better than 2000:1, according to the definition in Ref. [28].

About 54% of the backward THz electrical field strength was lost after the reflection on the silicon beam splitter surface. However, this design enables the normal reflection measurement, and the THz electric field at the sample position is greater than 30 kV/cm. The entire THz beam path is purged with dry nitrogen to eliminate absorption lines of water vapor.

To reach a broader THz bandwidth, instead of applying an 85 fs Ti-sapphire amplified laser, a 32 fs (FWHM) Ti-sapphire amplified laser is used (Coherent Legend Elite Duo USP) as the optical source. Figures 5(c) and 5(d) show the THz waveform and spectrum generated with the 32 fs amplified laser with 700 mW input power by the R-THz-ABCD spectrometer. The phonon resonances of the silicon beam splitter at 15, 18, and 22 THz [27,29] are clearly shown in Fig. 5(d). The spectrum covers the frequency range from 0.5 to 20 THz with 10% or greater of the maximum amplitude at 4.4 THz, and meets the noise floor of the measurement at approximately 35 THz.

1.2.5 System performance

The water vapor absorption, reflection features of dielectric materials and semiconductors are measured through the R-THz-ABCD spectrometer. An aluminum (Al) mirror is used as a reference due to its uniform and high reflectivity (over 98%) in the THz range. The front surface of the sample position is fixed, where the sample is mounted vertically and mechanically held on the backside of the sample target with an open window of 3 mm diameter. It is easy to switch the reference mirror and samples during the measurement. With special attention, the position error is less than 5 μm.

Figure 6 shows a waveform of water vapor absorption measured by R-THz-ABCD with a 73 ps scan length. In contrast to multiple reflections of crystal in EO sampling, the ABCD method avoids the multiple reflection echoes and provides a spectral resolution as high as 4×10^{-4} cm^{-1}. Figure 7 is the spectrum of water vapor absorption based on the measurement in Fig. 6 and compared with the result of FTIR measurement, in a 15% relative humidity. The two spectra are in good agreement. The magnification of Fig. 7 reveals water absorption peaks between 2 and 2.5 THz and these peaks are in a good agreement with previous reports [30,31].

With regards to dielectric materials, optical phonon resonances of a $CaCO_3$ crystal are shown in Fig. 3 and the reference measurements are performed. For the reflection module, the reference is taken based on the reflection from an Al mirror. Also, Fig. 8 reveals the phonon resonances of a 90° cut α-BBO crystal. The resonances of phonon modes shift when the optical axis of the α-BBO crystal rotates along the plane perpendicular to the THz beam path. Figures 8(a) and 8(b) show the waveforms at 0° and 90° of the optical axis with respect to pre-dominated THz p-polarization, respectively. Figures 8(c) and 8(d) show the related spectra in Figs. 8(a) and 8(b). As the angle is 0°, the major phonon modes are at 3.0 and 6.8 THz while major phonon modes are at 3.5, 4.1, 4.4, and 6.2 THz for 90° [32].

Regarding optical properties of semiconductors, the reflective spectra of several THz emitters such as n-type InAs, p-type InAs, GaAs, and GaP samples are measured with an 85 fs amplified laser. Figure 9(a) shows the reflectance of an n-type InAs sample with a doping concentration of 1.4×10^{17} cm^{-3}. The plasma resonance appears around 3 THz, which results in a larger reflection below 3 THz, and the phonon resonance is around 7.2 THz in agreement with previous publication [27]. Figure 9(b) shows the reflectance of a p-type InAs sample and its phonon resonance is around 7.2 THz.

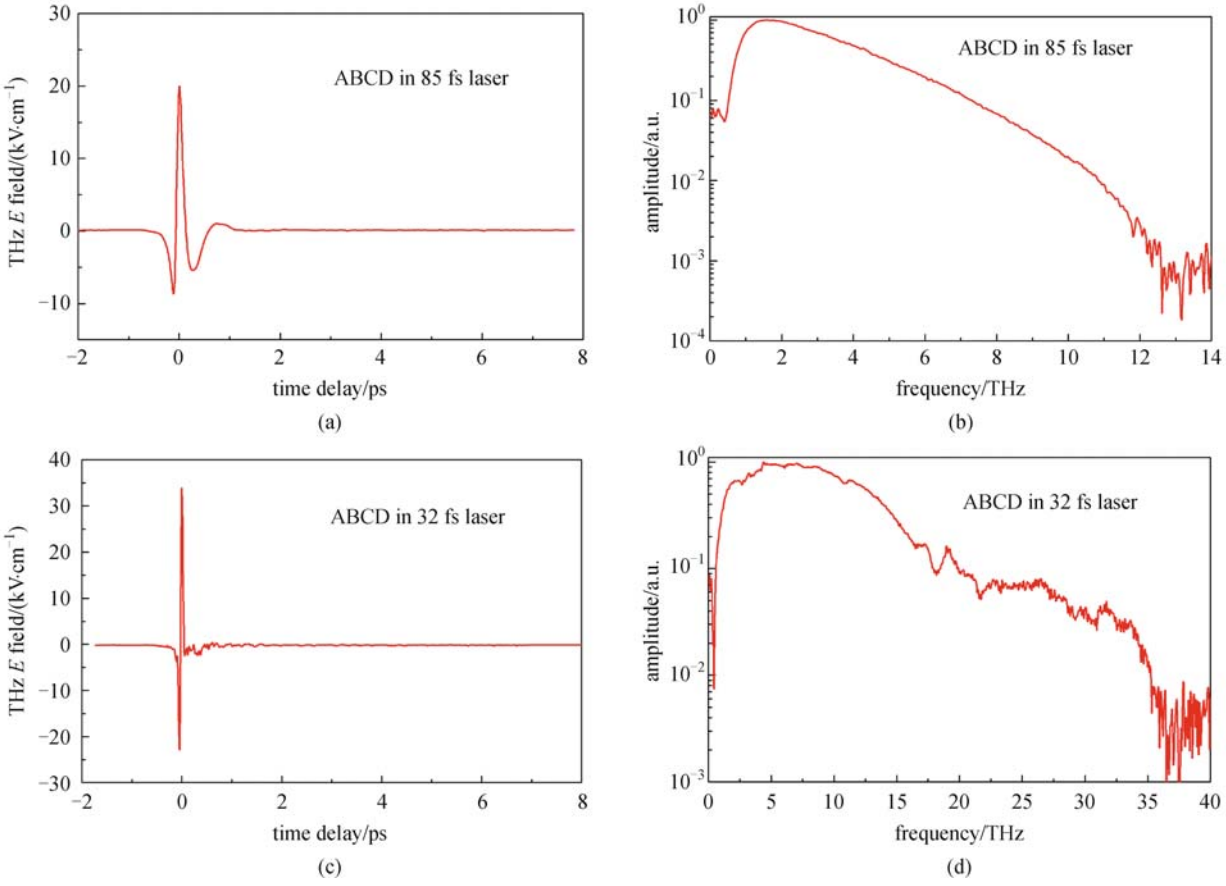

Fig. 5 (a) Measured time domain waveform and (b) Fourier transform spectrum of (a) with an 85 fs amplified laser; (c) measured time domain waveform and (d) Fourier transform spectrum of (c) with a 32 fs amplified laser with an R-THz-ABCD spectrometer

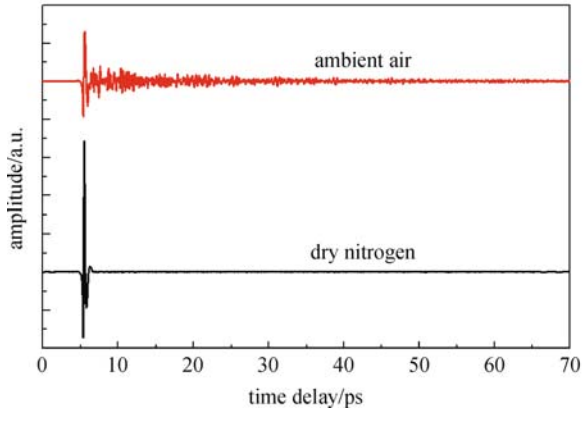

Fig. 6 Time-domain waveform of water vapor absorption measured with an R-THz-ABCD spectrometer. The relative humidity is ~15%

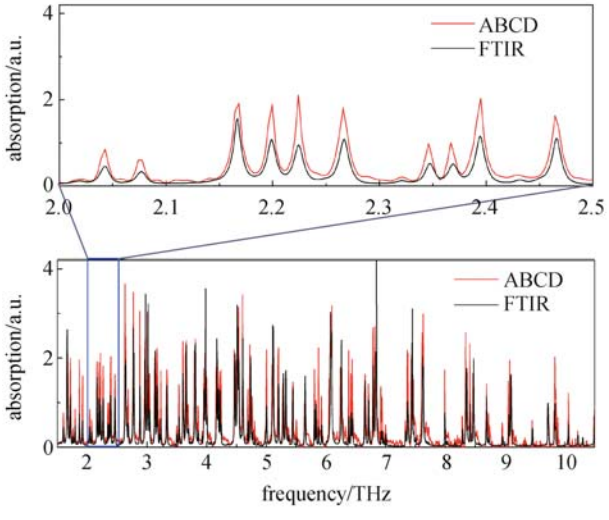

Fig. 7 Comparison of water vapor absorption spectra between R-THz-ABCD and FTIR measurement. The magnification shows the spectral range from 2 to 2.5 THz. The relative humidity is ~15%

1.2.6 Pulse steepening

In spite of operating with an 85 fs amplified laser, integrating a pulse steepening unit into the probe beam path, as shown in Fig. 10(a), provides an alternative method to obtain a shorter optical pulse duration and broader detection bandwidth. The beam steepening unit,

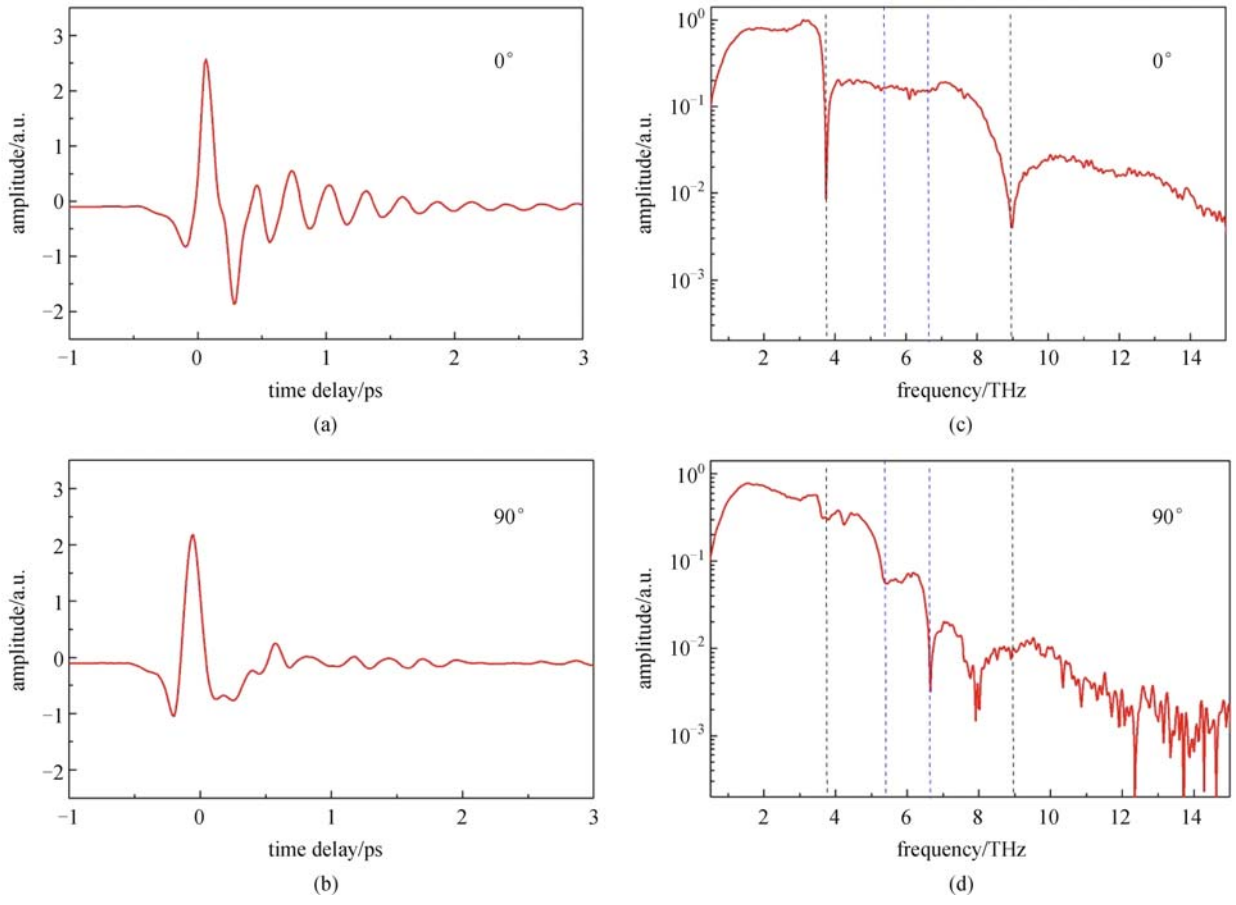

Fig. 8 (a) and (b) Measured reflective waveforms of a α-BBO crystal at an angle of 0° and 90°, respectively; (c) and (d) Fourier transform spectra of (a) and (b). The black dashed lines in (c) and (d) indicate the spectra dips due to the phonon resonances for 0° and the blue dashed lines for 90°

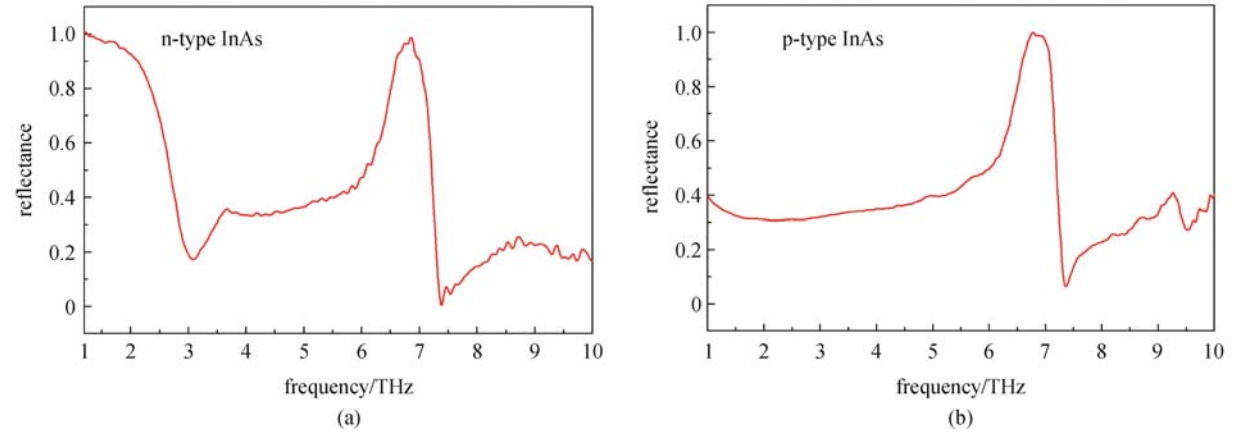

Fig. 9 (a) Reflectance of an n-type InAs sample. The plasma resonance is around 3 THz and the phonon resonance is around 7.2 THz; (b) reflectance of a p-type InAs sample. The phonon resonance is around 7.2 THz

which consists of two convex lenses with a focal length of 8.8 and 7.6 cm respectively, pre-focuses the probe beam to generate air plasma and then collimates the beam. The optical pulse duration decreases and bandwidth broadens after passing through the air plasma [33]. Figure 10(b) shows a usable bandwidth of the R-THz-ABCD spectrometer continuously from 0.5 to 20 THz. This method expands the detected THz bandwidth up to 20 THz with an 85 fs laser while the spectrum has dips at 18 THz, which are phonon absorption of the silicon beam splitter.

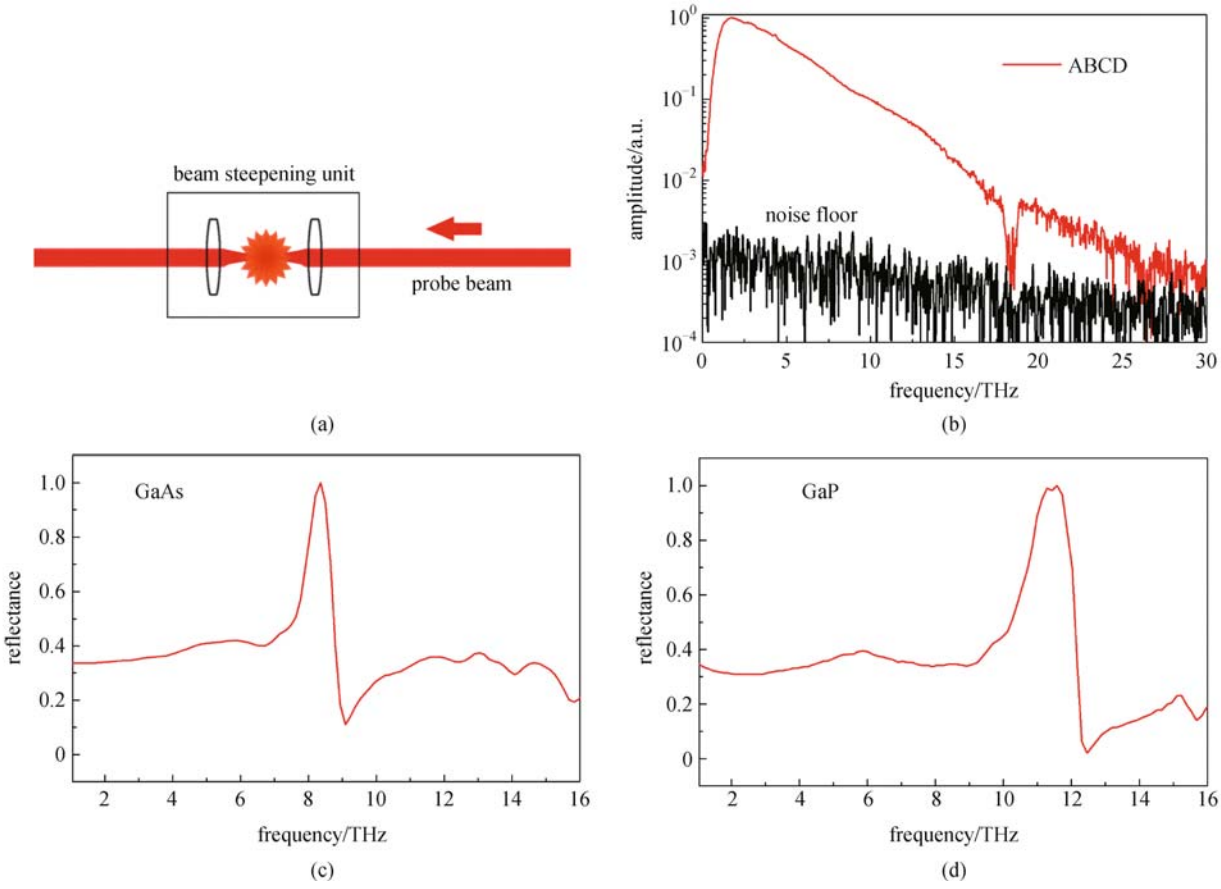

Fig. 10 (a) Beam steepening unit consists of two convex lenses; (b) Fourier transform spectrum (red curve) and noise floor (black curve) measured with adding the beam steepening unit; (c) reflectance of a GaAs sample with the phonon resonance around 8.8 THz; (d) reflectance of a GaP sample with the phonon resonance around 11 THz

Figure 10(c) shows the reflectance of a GaAs crystal with the phonon resonance around 8.8 THz [34]. Figure 10(d) shows the reflectance of a GaP crystal with the phonon resonance around 11 THz [34].

1.2.7 Comparison: R-THz-ABCD, traditional THz-TDS, and FTIR

According to above results, the uniqueness and advantage of the R-THz-ABCD spectroscopy, traditional THz-TDS, and FTIR spectroscopy are comprehensively compared from far-infrared to mid-infrared range. THz-TDS with high SNR has been developed over the last two decades by Wu et al. [35]. However, the useful bandwidth in the THz range is limited (< 5 THz with a ZnTe sensor) and the peak electric field is weak ($<$ several kV/cm). On the other hand, FTIR spectroscopy has been transformed to a commercial product which provides a useful bandwidth from far-infrared to visible range. However, the peak electric field is much weaker than THz-TDS, and it is difficult to perform time-resolved measurements [36].

In an 85 fs amplified laser, the R-THz-ABCD system provides a broad bandwidth (0.5 – 10 THz with 10% or greater of the maximum amplitude at 1.72 THz referred to Fig. 10(b), high peak THz field (> 30 kV/cm), as well as time-resolved measurements. Table 1 lists a series of comparisons including radiation source, detector, DR, bandwidth, resolution, peak power, and data acquisition time. In terms of SNR according to the definition of Ref. [28], the SNR as a function of frequency in both R-THz-ABCD and FTIR is shown in Fig. 11.

Here, a Bruker IFS 66v/S spectrometer is utilized for comparison where a mercury lamp as the source and DTGS as the detector are used. In a nine-time scan average, several parameters are selected, such as a 0.6 cm^{-1} resolution, a T222 beam splitter, a 6 mm aperture setting, and a single-sided acquisition mode. For the R-THz-ABCD spectrometer, the resolution at 1.6 cm^{-1} and a 100 ms lock-in amplifier time constant are set in a nine-time scan average. Figure 11 clearly shows the R-THz-ABCD with higher SNR below 5.4 THz compared to FTIR. Even though the SNR of the R-THz-ABCD

Table 1 Comparison of R-THz-ABCD, traditional THz-TDS, and FTIR

source	R-THz-ABCD (85 fs laser)	traditional THz-TDS	FTIR (Bruker IFS 66v/S)
	dry nitrogen	ZnTe	mercury lamp
detector	dry nitrogen	ZnTe	DTGS
DR of power (< 3THz)	$> 10^6$	$> 10^8$	~300
bandwidth (10% or greater of peak amplitude)	0.5 – 10 THz	0.1 – 3 THz	far to mid-infrared
resolution	~0.1 cm^{-1}	~0.1 cm^{-1}	~0.1 cm^{-1}
peak power	6×10^4 W	2×10^3 W (amplified laser)	1×10^{-7} W
data acquisition time	seconds or minutes	minutes	minutes
uniqueness	time resolved & broad bandwidth	time resolved & high SNR	broad bandwidth

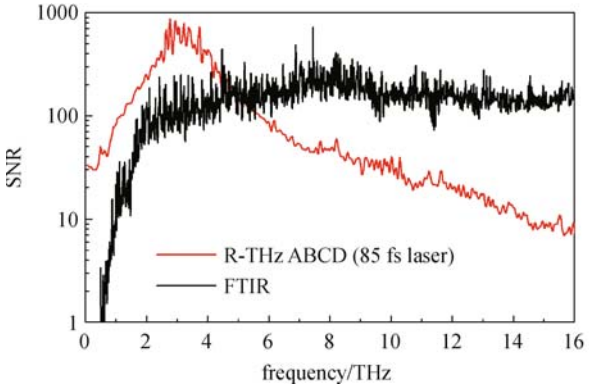

Fig. 11 SNR of R-THz-ABCD (red curve) in a nine-time scan average and SNR of FTIR (black curve) in a nine-time scan average

decreases with frequency after 3 THz, it still has good SNR until 16 THz.

1.2.8 Summary

A broad bandwidth (0.5 – 35 THz in a 32 fs laser), high peak electrical field (> 30 kV/cm), high peak DR (> 2000), and table-top R-THz-ABCD spectrometer has been realized. It provides time-resolved optical gating and absorption-free measurement for bulk materials. Optical properties of dielectric materials and semiconductors are retrieved with the spectrometer. By integrating a pulse steepening unit, the bandwidth covers the entire THz gap and enters the mid-infrared range with an 85 fs amplified laser. Finally, a comprehensive comparison of R-THz-ABCD, traditional THz-TDS, and FTIR is performed. Compared to transitional THz-TDS, R-THz-ABCD has a remarkably broad bandwidth as well as at least one order larger peak THz field. Compared to FTIR, it provides time-resolved optical gating and several orders larger peak electric field.

The design and performance of the R-THz-ABCD spectrometer open a bright outlook for further scientific study. In Sections 2 and 3, nonlinear carrier dynamics in semiconductors under intense THz field excitation will be performed with a THz pump-THz probe technique. Several veiled phenomena regarding the high electric field excitation and short time scale responses in semiconductors are reported.

2 Semiconductor nonlinearity I: carrier dynamics

THz pulses inducing intervalley scattering and impact ionization in doped InAs crystals by THz pump-THz probe measurements are reported in this section. Two competing mechanisms are observed by changing the impurity doping type of the semiconductors and varying the strength of the THz field. For p-doped InAs, a cascaded carrier generation dominates, while for n-doped InAs, both mechanisms have to be considered. Electron fractional occupancy between the Γ and L valleys is estimated at different field strengths.

2.1 Background review

The high-field transportation properties of electrons in semiconductors are essential for semiconductor devices such as avalanche photodetectors, impact ionization avalanche transit-time (IMPATT) diodes, and high-power field-effect transistors [37]. Several theoretical and experimental studies have addressed the electrical properties regarding carrier dynamics for narrow bandgap semiconductors [38–41]. In the 1990s, researchers applied far-infrared (FIR) radiation generated with a free electron laser or with a transversely excited atmosphere (TEA) CO_2 laser on semiconductors to monitor the ionization of impurities [42,43]. With different AC-field excitation, the charge density increases abruptly for FIR intensities above a threshold value for ionization.

However, the continuous FIR source such as a TEA CO_2 laser cannot provide enough THz field strength or suitable excitation bandwidth to modulate nonlinear responses in solids, while a free electron laser brings the problem of its giant facility. Nevertheless, recently as a result of the plentiful developments of intense THz pulse sources on table-top systems [1–4,13,14] as described in Section 1,

THz waves are now a powerful tool for studying transient nonlinear dynamics.

Regarding InAs, it is used as a traditional THz wave source upon irradiation with femtosecond laser pulses because of its high mobility (~30000 $cm^2 \cdot V^{-1} \cdot s^{-1}$) and narrow bandgap (~0.36 eV at 300 K) properties. Although the electrical properties of InAs with an applied direct current (DC) field have been reported, transient carrier dynamics in correspondence to sub-picosecond time scale is unexplored. Furthermore, the unique band structure of InAs makes its bandgap and the electron valley transfer energy (Γ and L valleys) close, which results in the impact ionization and intervalley scattering competing against each other with high field excitation. The two mechanisms are observed on sub-picosecond time scales by varying the impurity doping type of the semiconductors and the strength of the THz field, which is described as follows.

2.2 Physical mechanisms

2.2.1 Impact ionization

Impact ionization attracts a lot of attention in semiconductor devices especially related to high-field carrier transportation. When a free carrier gains energy, it might collide with a bound carrier, freeing the latter in the process. If the excess carrier has enough energy, it will collide with a bound carrier again to form a cascaded carrier generation [44]. In semiconductors, when the electric field is increased above a certain value, electrons from the conduction band gain enough energy to excite the electron-hole pairs in the valence band. The threshold energy has to be greater than the bandgap [37]. The impact ionization process is illustrated in Fig. 12.

2.2.2 Intervalley scattering

At very high electric field, electrons in the conduction bands transfer from a lower valley to satellite valleys, known as intervalley scattering. Figure 13 demonstrates the electron valley transfer. The effective mass of electrons is different from valley to valley, which results in the mobility change when intervalley scattering happens. Su et al. have reported THz-pulse-induced intervalley scattering of electrons between the Γ and L valleys in GaAs [45]. Due to a smaller energy required for electron valley transfer (0.29 eV), compared to the bandgap (1.43 eV) in GaAs, the intervalley scattering has been observed by an optical pump-THz probe technique.

2.2.3 Band structures

Comparing with the band structures of GaAs and InSb, the band structure of InAs is unique that the electron valley transfer energy (considering Γ and L valleys) is two times of its bandgap. For GaAs, its bandgap is five times of the energy for electron valley transfer; for InSb, the energy for electron valley transfer is three times of the bandgap. The band diagrams of these three materials are shown in Fig. 14.

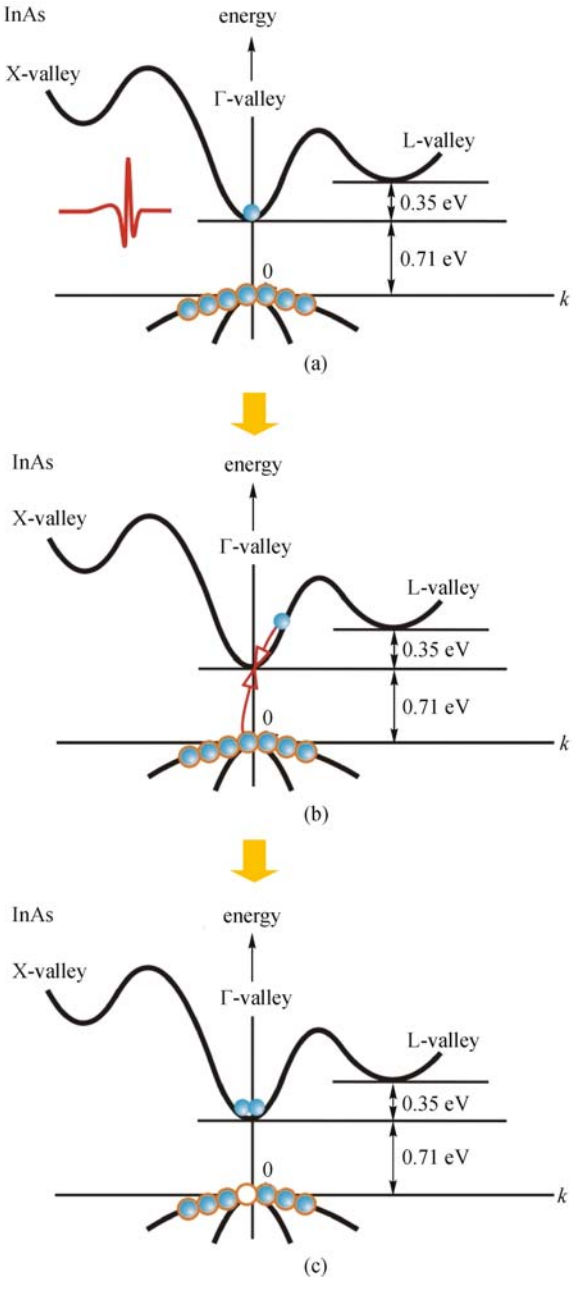

Fig. 12 Illustration of impact ionization process. The electron in conduction band gains energy from a THz pulse (a) and generates an electron-hole pair (b); (c) effective mass of holes is much larger than electrons, so only the impact ionization from electrons is considered

Therefore, it would be interesting to study the electron dynamics as intense THz pulses excite these materials.

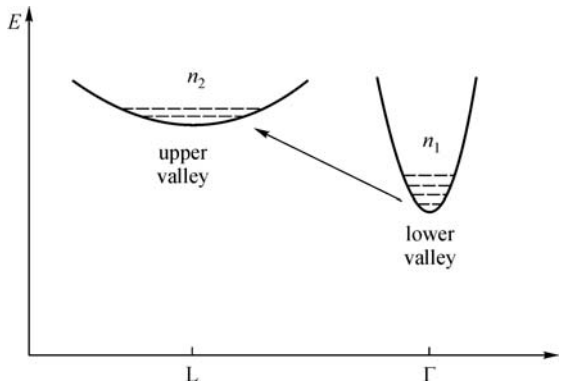

Fig. 13 Intervalley scattering of electrons between two valleys

Especially for the InAs, the transient carrier dynamics is still unexplored.

2.3 Experimental design

Instead of utilizing the commonly-used transmission geometry for THz pump/probe experiments, reflection geometry with high sensitivity for bulk materials is applied. For the narrow bandgap semiconductors with high electrical conductivity, the transmitted THz field is attenuated severely after passing through bulk samples. Therefore, reflection geometry is preferred. The experimental setup is shown in Fig. 15 and details are described in Section 1. A regenerative Ti:sapphire amplified laser with 3 mJ pulse energy, 800 nm central wavelength, 35 fs pulse duration, and 1 kHz repetition rate is the laser source. THz waves, with an electric field up to 110 kV/cm on the sample, are generated during the gas ionization process induced by mixing femtosecond pulses with 800 and 400 nm wavelengths.

The investigated samples are bulk n- or p-doped InAs with carrier concentrations of 10^{17} or 10^{18} cm^{-3}. To compare with previous findings, n-doped GaAs of 10^{17} cm^{-3} and n-doped InSb of 10^{14} cm^{-3} are also measured to demonstrate carrier transport. For the InSb sample, although the doping concentration is 10^{14} cm^{-3}, thermal ionization at room temperature makes the carrier concentration around 10^{16} cm^{-3}. The samples are excited by single-cycle THz pump pulses with a duration of approximately 150 fs. The THz probe pulses (15 kV/cm) with the same pulse duration of the pump reflected from the samples is EO sampled with a 220-μm thick, <110> -orientation GaP crystal. A mechanical chopper is inserted into the system to modulate the output of the THz probe beam. All experiments were performed at room temperatures and purged by dry nitrogen.

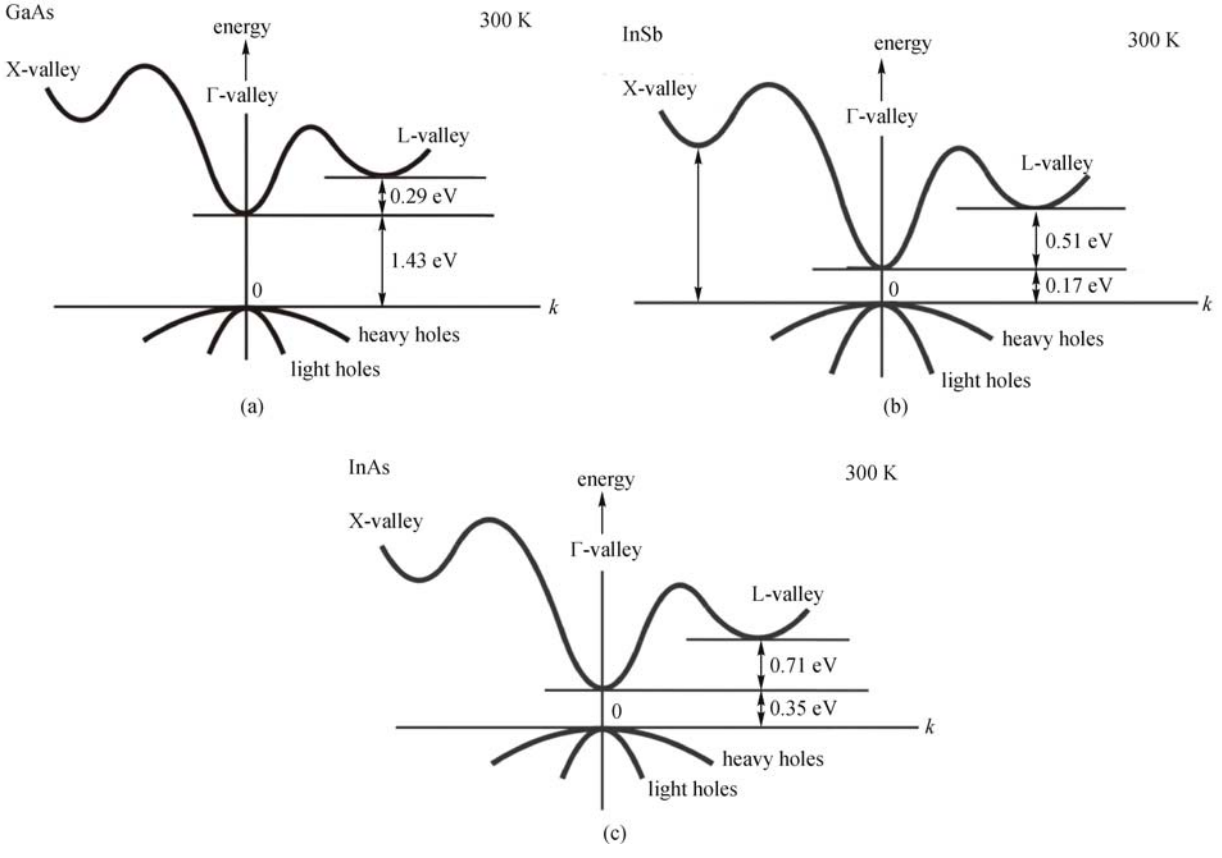

Fig. 14 Band structures of GaAs (a), InSb (b), and InAs (c) at 300 K

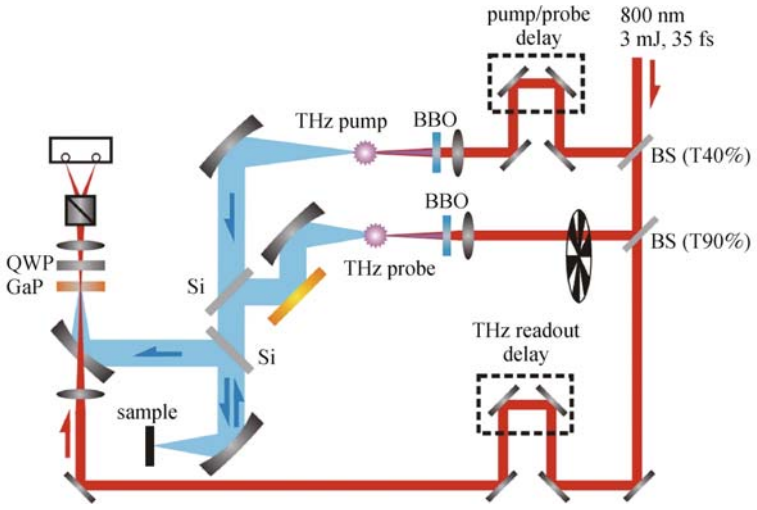

Fig. 15 Schematic illustration of a reflective pump/probe setup. The THz pump/probe pulses are generated by air plasmas, and the THz probe pulses are detected by EO sampling. BS, beam splitter; QWP, quarter-wave plate. The full-width of half maximum of the THz beam diameter at sample is 0.75 mm, measured with a knife-edge method

2.4 Experimental observation

2.4.1 Terahertz pump-terahertz probe technique

Figure 16 shows the experimental observations of carrier dynamics in p-doped InAs and n-doped InSb crystals. The normalized reflections of the probe peak field are measured as a function of pump/probe delay τ. When THz pump pulses arrive earlier than THz probe pulses, defined as $\tau > 0$, a reflection increase of p-doped InAs crystals is measured as shown in Fig. 16(a). The phenomenon is due to energetic electrons from the conduction band exciting electron-hole pairs in the valence band, known as impact ionization [44]. More carriers generated lead to a higher conductivity, and the reflection increases following Eq. (3).

$$r \propto \sigma = q\mu N, \tag{3}$$

where r is the reflection, σ is the electrical conductivity, q is the electron charge, μ is the carrier mobility, and N is the carrier density. According to the mass-action law [37],

$$pn = n_i^2, \tag{4}$$

where n_i ($\sim 10^{15}\,\mathrm{cm}^{-3}$ at 300 K for InAs) is the intrinsic carrier density, and p and n is hole and electron density, respectively, the electron density in InAs with p-doped $10^{18}\,\mathrm{cm}^{-3}$ must be less than $10^{17}\,\mathrm{cm}^{-3}$. Fewer electrons in this heavily doped InAs ($10^{18}\,\mathrm{cm}^{-3}$) result in a smaller generation of electron-hole pairs, which leads to a weaker reflection increase (3.6%) in the InAs crystal of $10^{18}\,\mathrm{cm}^{-3}$ as compared to $10^{17}\,\mathrm{cm}^{-3}$ (13.5%) as shown in Fig. 16(a). For comparison, n-doped InSb, whose bandgap (~ 0.17 eV at 300 K) is smaller than InAs, is also measured to demonstrate impact ionization and shown in Fig. 16(b). The reflection drop at $\tau \sim 0$ is caused by a decrease in the

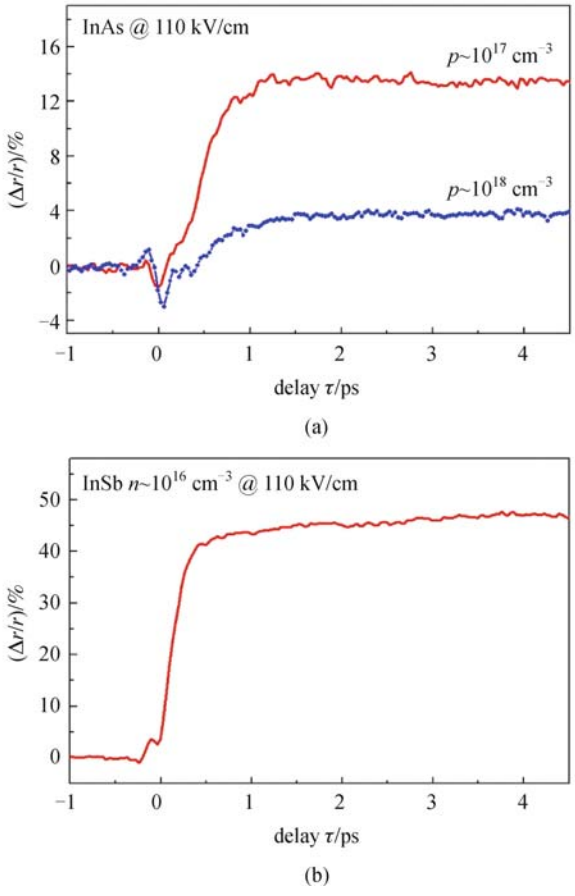

Fig. 16 Normalized reflection of the THz probe peak field as a function of delay τ. The reflection increases after $\tau > 0$ due to a cascaded carrier generation. (a) p-doped InAs crystals with doping concentrations of $10^{17}\,\mathrm{cm}^{-3}$ (solid line) and $10^{18}\,\mathrm{cm}^{-3}$ (solid line with dots); (b) n-doped InSb crystal with a doping concentration of $10^{16}\,\mathrm{cm}^{-3}$

mobility of the hot electrons as a result of the strong nonparabolicity of the Γ valley in the conduction band of InAs and InSb [46].

On the contrary to the characteristic of p-doped InAs crystals, the n-doped InAs crystal shows that the reflection suddenly decreases and then increases slowly after pump/probe delay $\tau > 0$, as shown in Fig. 17(a). The phenomenon is explained with two mechanisms: intervalley scattering [45,47] and impact ionization [41,43,44,46,48]. Arabshahi and Golafrooz used an ensemble Monte Carlo simulation to predict inverted electron distribution due to intervalley electron transfer [49]. In their calculation without considering impact ionization for bulk InAs of n-doped 10^{17} cm^{-3}, the fractional occupation of the Γ and L valleys are already inverted when an applied electric field is 25 kV/cm. However, the electron effective mass in the L valley is one order heavier than that in the Γ valley. Therefore, when electrons transfer to the satellite valley, the reflection decreases suddenly in correspondence to the carrier mobility.

$$\mu \propto \frac{1}{m^*}, \tag{5}$$

where m^* is the effective mass of the carrier. The simulation of the electron distribution between the Γ and L valleys [49] explains the decrease in reflection when pump and probe pulses overlap, as shown in Fig. 17(a).

Nevertheless, the energetic electrons in the conduction bands, which have high kinetic energy under strong electric field, also excite electron-hole pairs from the valence band. In Fig. 17(a), when the THz pump field is 110 kV/cm, the normalized reflection slowly increases over 6% with pump/probe delay $\tau > 0$. However, when the THz pump field is 90 kV/cm, the remained kinetic energy of electrons after valley transfer makes it difficult to generate electron-hole pairs. Therefore, the reflection remains smaller than the unperturbed reflection with pump/probe delay $\tau > 0$. It is worth noting that the interaction of energetic electrons and a phonon field leads to the modulation ripple as shown in Fig. 17(a). This intrinsic phenomenon will be detailed explained in Section 3. With regards to the intervalley scattering, n-doped GaAs also shows the electron transfer between Γ and L valleys which has been reported previously [45,47] and is reproduced in Fig. 17(b).

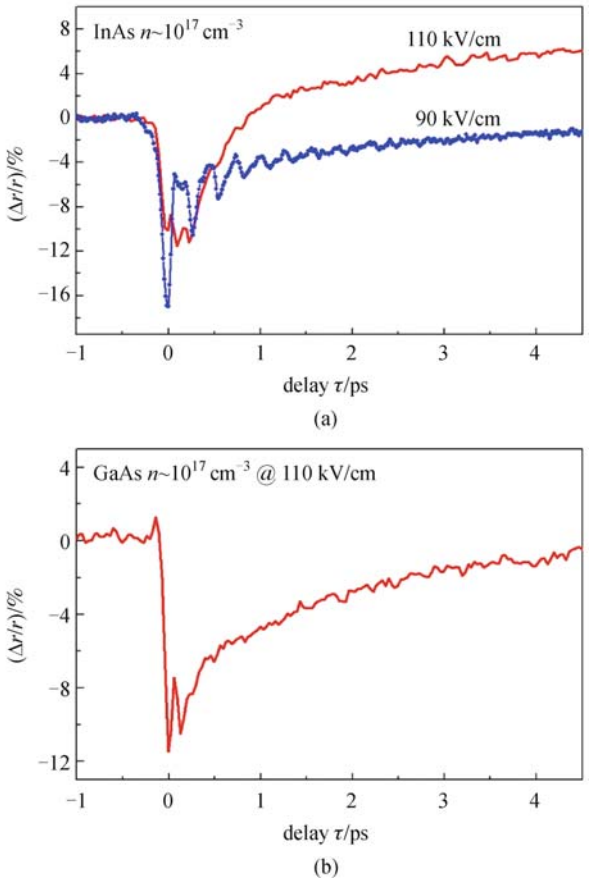

Fig. 17 (a) n-doped InAs crystal with a doping concentration of 10^{17} cm^{-3} at different THz pump field excitation, 110 kV/cm (solid line) and 90 kV/cm (solid line with dots); (b) n-doped GaAs crystal with a doping concentration of 10^{17} cm^{-3}. The reflection decreases with $\tau > 0$ due to carrier intervalley scattering

2.4.2 Reflection measurement: electron valley occupancy

Even though the EO sampling by a GaP crystal provides a two times higher signal-to-noise ratio than a THz-ABCD method [6,7], the detectable bandwidth is limited to 8 THz due to the phonon absorption of the GaP crystal. To monitor the phonon and plasma responses in a broader frequency range, we utilize THz-ABCD which provides a 0.5–12 THz frequency range in this experiment. Figure 18 shows the reflection of 10^{17} cm^{-3} n-doped InAs measured with a single THz beam at 30, 44, 63 and 90 kV/cm field

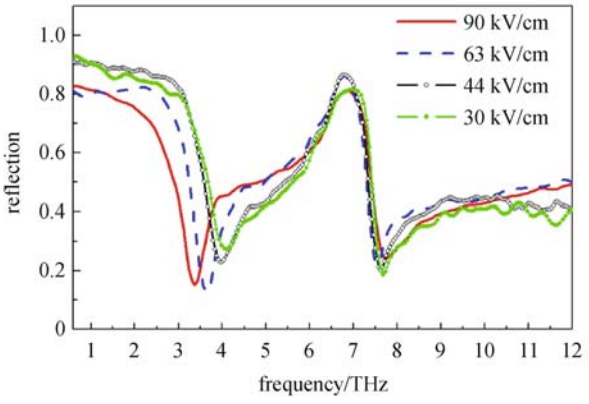

Fig. 18 Reflection measurement with THz-ABCD. The reflections are of different THz field strengths in n-doped InAs

strengths, respectively. According to plasma oscillation frequency,

$$\omega_{\mathrm{p}} = \sqrt{\frac{Nq^2}{m^* \varepsilon_\infty \varepsilon_0}}, \tag{6}$$

where ε_0 is the permittivity in a vacuum and ε is the relative permittivity, the plasma resonance of n-doped InAs of 10^{17} cm^{-3} is around 5.6 THz. In Fig. 18, it can be clearly seen that plasma resonance shifts from 4.1 to 3.4 THz as the electric field increases from 30 to 90 kV/cm while the optical phonon resonance remains unchanged at around 7 THz. This plasma resonance shift is due to partial electron transfer from the Γ valley to the L valley. When electrons are scattered into the satellite valley, their effective mass becomes larger and causes the plasma resonance shift to a lower frequency.

The electron population between the Γ and L valleys in different field strengths is estimated by the plasma resonances in Fig. 18. Three assumptions are proposed. First, the free carrier density is assumed the same at different THz field strengths. Even though the impact ionization generates electron-hole pairs, the normalized reflection increase is only 6% at a field strength of 110 kV/cm. Second, electron transfer between Γ and L valleys are only considered. E_{X} = 1.37 eV is 4 times the value of the bandgap, whereas E_{L} is 3 times the value of the bandgap. The X valley is not considered in this estimation. Third, electrons in the same valley have the same effective mass. According to Eq. (6) and the parameters in Ref. [12], the fractional occupation of Γ and L valleys is estimated, as shown in Fig. 19. In this work, a short pulse excitation is utilized instead of a static electric field so that the threshold for intervalley transfer is easily reached when impact ionization and intervalley scattering compete against each other.

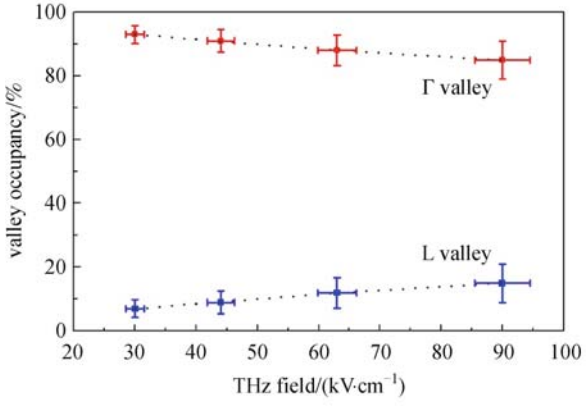

Fig. 19 Experimental estimation of electron fractional occupancy between Γ and L valleys at different THz field strengths according to the plasma resonances in Fig. 18. The circular and square dots are experimental data of the Γ and L valleys, respectively. The dotted lines are fitting curves

2.5 Summary

Impact ionization and intervalley scattering within a sub-picosecond time scale for bulk InAs are reported. For p-doped InAs, a cascaded carrier generation dominates, while for n-doped InAs, both mechanisms have to be considered. With a single THz beam excitation on the n-doped InAs at different field strengths, the electron fractional occupation between the Γ and L valleys is estimated, which reflects the recent Monte Carlo simulation.

3 Semiconductor nonlinearity II: polaron modulation

This section addresses the electron-phonon coupling on a sub-picosecond time scale considering intense THz field excitation. An electron interacts with its surrounding lattice distortion, known as the Fröhlich polaron [50]. The polaron motion perturbed with intense field excitation shows a nonlinear response.

In this study, by utilizing an all-THz pump/probe technique, the coherent polaron vibrations in n-doped III-V semiconductors are clearly demonstrated through the modulations of reflection. The interaction between energetic electrons and the phonon field on the sub-picosecond time scale is verified, and it is shown that this interaction applies for acoustic phonon modes. This work provides a unique method to diagnose the overtones of two transverse acoustic phonon responses of semiconductors in a nonlinear regime, and therefore bridges the relationship between the infrared and Raman spectroscopy.

3.1 Background review

Recently, several major research topics involving the interaction of strong THz transients with semiconductors are reported. For example, Kuehn et al. showed coherent ballistic transport of electrons by time-resolved high-field THz measurements [51,52]; the strong electric field drives the polaron in a GaAs crystal into a highly nonlinear region where the coherent phonon vibration persists for several hundred femtoseconds, which causes electron nonlinear radiation [53].

In spite of the previous polaron studies, the electron-phonon field coupling under intense THz field excitation on ultrashort timescales has not been extensively investigated. In this section, electrons in n-doped semiconductors are driven into reverse motion by high-field THz pulses. The THz pump pulses drive the electrons into the same or opposite polarities with respect to the electric field of THz probe pulses. By utilizing the all-THz pump/probe scheme, the coherent polaron vibrations are clearly demonstrated through the modulations of reflection.

3.2 Experimental design

A reflective THz pump/probe scheme, similar to the setup in Fig. 15, is utilized to study the semiconductor carrier dynamics, as shown in Fig. 20. A regenerative Ti:sapphire amplified laser with 3 mJ pulse energy, 800 nm central wavelength, 35 fs pulse duration, and 1 kHz repetition rate is utilized for the optical source. Intense THz waves, with an electric field up to 100 kV/cm on the sample, are generated during gas ionization processes induced by mixing femtosecond pulses with 800 and 400 nm wavelengths. Samples investigated are n-doped InSb crystals with carrier concentrations of 10^{14} and 10^{16} cm^{-3} as well as n-doped InAs crystals of 10^{16} and 10^{17} cm^{-3}. They are excited by single-cycle THz pump pulses with duration of approximately 150 fs. The THz probe pulses (15 kV/cm) with the same pulse duration of the pump reflected from samples are EO sampled with a GaP crystal.

A mechanical chopper is inserted into the probe beam path to modulate its output. Only chopping the probe beam, the absolute change of reflection is retrieved. However, integrating a frequency divider which chops the pump (f/3) and the probe (f/2), the reflection with f/6 is measured to get a better SNR, where f is the laser repetition rate. To monitor a broader frequency range of the nonlinear polaron responses, we also utilize THz-ABCD, as shown in the inset of Fig. 20, providing a 0.5 – 10 THz frequency range in this experiment. All experiments were performed at room temperature and purged by dry nitrogen gas.

3.3 Physical explanation of polaron dynamics

With strong THz pump fields illuminating the samples as well as controllable pulse polarities, intrinsic electrons in n-doped semiconductors are accelerated in different ways. The energetic electrons interacting with the phonon cloud,

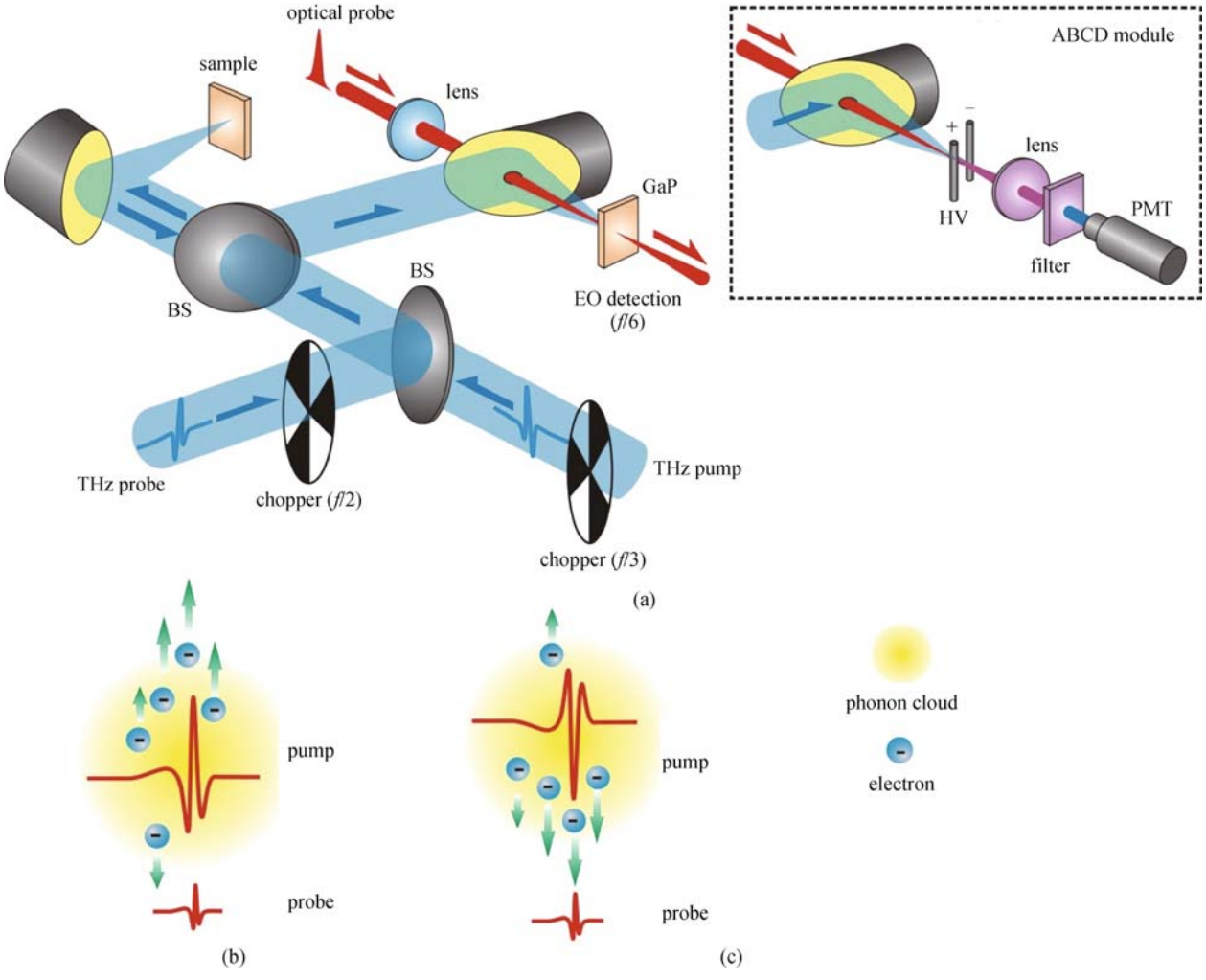

Fig. 20 (a) Schematic illustration of the measurement setup. The THz pump/probe pulses are generated in air plasmas and detected by EO sampling or by ABCD (the black-dashed inset). The polarities of the pump/probe pulses are controlled independently. PMT, photomultiplier tube; BS, beam splitter; HV, high voltage; (b) and (c) electron motions driven by different polarities between THz pump/probe pulses, parallel and antiparallel, respectively (by rotating the BBO crystal in the pump beam to change the polarity)

known as Fröhlich coupling, start to escape from the phonon field after the high field excitation [53–55]. Therefore, when the THz pump pulses arrive earlier than the THz probe pulses defined as $\tau > 0$, the pump pulses with polarities the same (Fig. 20(b)) or opposite (Fig. 20 (c)) to the fixed polarity of the probe pulses drive the electrons into reverse motions.

Furthermore, the energetic electrons transfer the energy to the lattice with the coulomb potential, leading to the coherent phonon oscillation. However, under the intense THz field excitation, the phonon cloud is too slow to follow the strongly accelerated electrons so that the electrons escape and evolve "nakedly" in the ballistic regime [51,54]. The coherent phonon excitation, inducing the strongly distorted electron-phonon potentials [53], results in electron nonlinear motions.

3.4 Experimental verification and mathematical description

3.4.1 Coherent polaron oscillation

Figure 21 shows experimental observations of coherent polaron oscillations. The normalized reflection changes of the probe peak field are measured as a function of pump/probe delay τ. Figures 21(a) and 21(b) show the modulated reflections with reverse polarities of the pump pulses (parallel and antiparallel polarities between THz pump/probe pulses). The THz pump and probe fields on the samples are 75 and 15 kV/cm, respectively. In Fig. 21(a) the rising curves of the reflection (after $\tau > 0$) are due to impact ionization of the InSb crystal of 10^{14} cm^{-3} [46,48], while in Fig. 21(b) the falling curves (after $\tau < 0$) are due to intervalley scattering of the InAs crystal of 10^{17} cm^{-3} [56].

The strongly distorted electron-phonon potential excited by THz pump pulses [53] in the parallel and antiparallel cases results in the opposite polaron oscillations observed in Figs. 21(a) and 21(b). Such polaron oscillations are attributed to the nonlinear term of the electron velocity with an external field that is expressed as

$$v_e(E) = v_e(E_0) + \frac{\partial v_e(E_0)}{\partial E}(E - E_0) + \cdots, \qquad (7)$$

where v_e is the electron velocity, E_0 is the pump electric field, and E is the local electric field including THz pump field, THz probe field, and the nonlinear radiation field of electrons. The first term on the right hand side of Eq. (7) corresponds to the Drude model which is $v_e(E_0) = \mu_0 E_0$. μ_0 is the constant mobility in the linear region. The second term on the right hand side of Eq. (7) is related to the nonlinear electron oscillation. The differential mobility is defined as

$$\mu_{\text{diff}}(v_e) = \left[\frac{\partial v_e(E_0)}{\partial E}\right]\left(1 - \frac{E_0}{E}\right). \qquad (8)$$

Since the THz pump-induced probe change is independent on the first term of Eq. (7), where μ_0 is a constant, the pump/probe measurement only measures the second term of Eq. (7). Moreover, the reflection is proportional to the conductivity of samples and the conductivity is read as $\sigma = e\mu n$, where e is electron charge, μ is mobility, and n is free carrier density. Therefore, the resulting change of the modulated reflection,

$$\Delta r \propto \mu_{\text{diff}}(v_e), \qquad (9)$$

is proportional to the amplitude of the differential mobility [53]. The polarity control between the pump/probe pulses makes the total electric field (THz pump and probe fields) E slightly larger than E_0 (parallel case) or slightly smaller than E_0 (antiparallel case), which flips over the oscillatory features of the reflection (around $\tau = 0$) as shown in Figs. 21(a) and 21(b).

Figures 21(c) and 21(d) demonstrate the oscillatory features at different doping concentrations. For the InSb crystals, as a result of the thermal-ionization of carriers [48], the samples of 10^{14} and 10^{16} cm^{-3} have a similar oscillatory feature and the oscillatory frequency is around 2 THz. For the InAs crystals, the vibration modes are different from the two doping concentrations of 10^{17} and 10^{16} cm^{-3}. The vibration mode of the 10^{17} cm^{-3} is around 3.4 THz, as shown in Fig. 21(e), while two vibration modes (1.6 and 3.4 THz) appear at the 10^{16} cm^{-3}, as shown in Fig. 21(f). It is worth noting that an electron-phonon coupling mode at 3.4 THz is observed in the both doping concentrations. Nevertheless, the 10^{16} cm^{-3} shows an extra vibration mode at 1.6 THz.

3.4.2 Differential method

To further consider the nature of coherent oscillations in Fig. 21, Figs. 22(a) and 22(b) show the waveforms retrieved by subtraction of the two curves in parallel and antiparallel cases of each sample according to Figs. 21(a) and 21(b). The monotonic reflection changes due to impact ionization or intervalley scattering are eliminated whereas the coherent polaron oscillations (around $\tau = 0$) are doubled. Figures 22(c) and 22(d) show the Fourier transforms of the waveforms according to Figs. 22(a) and 22(b), respectively.

The central frequency of the oscillation for the InSb sample is around 2 THz, while for the InAs sample it is around 3.6 THz. These oscillation frequencies are attributed to the excitations of the overtones of two transverse acoustic (2TA) phonons [57–59]. In earlier publications, the overtones of two-phonon density of states, calculated with the overlap-valence-shell (OVS) model [60], and second-order acoustic Raman spectra [58,59] both showed dominant response frequencies at around 2.2 THz (2TA) and 3.2 THz (2TA) for InSb and InAs, respectively. Therefore, the impulsive electrons transfer energy to the lattice at 2TA phonon modes to further modulate the reflection.

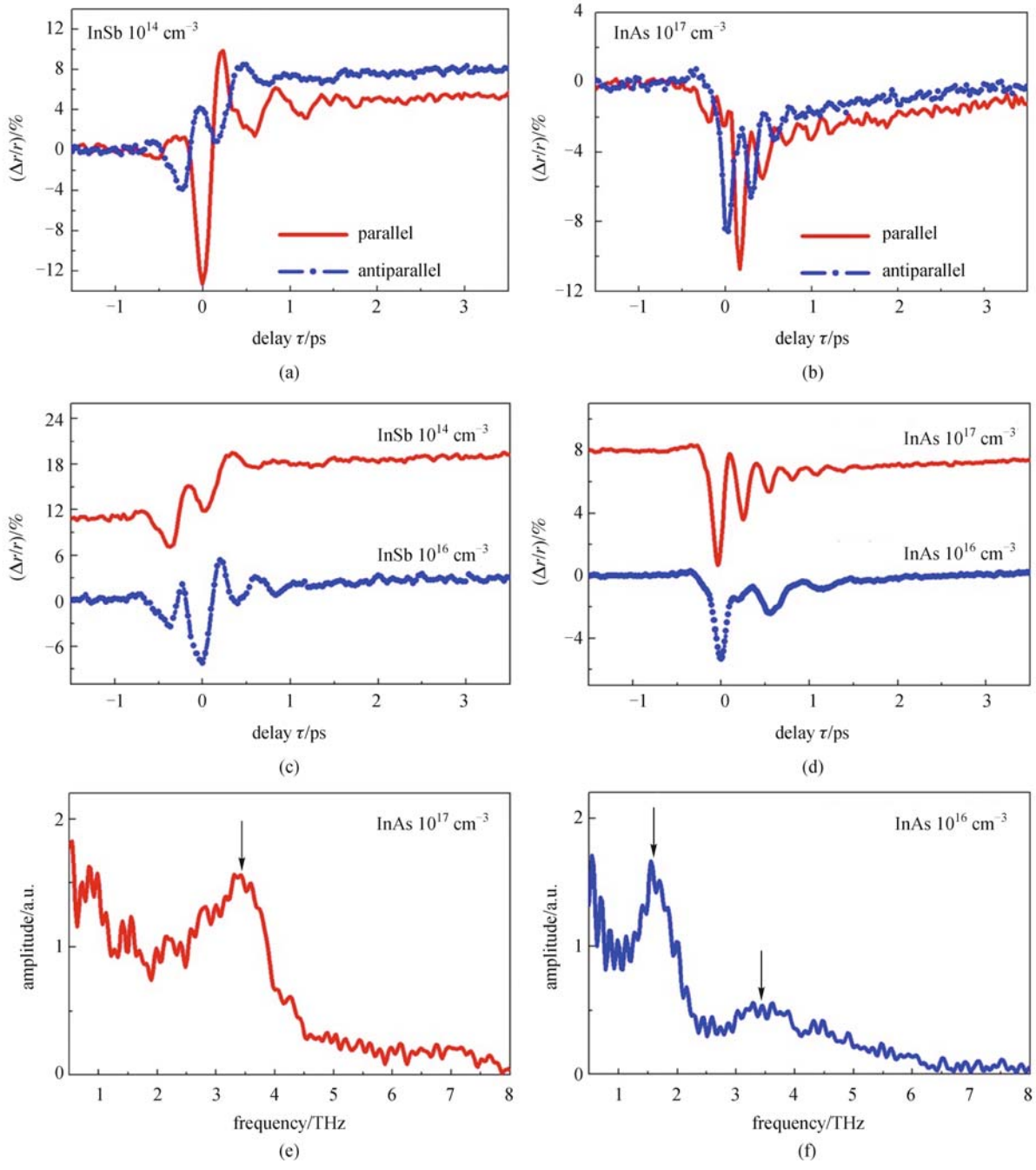

Fig. 21 Experimental results of coherent polaron oscillations with EO detection. (a) and (b) InSb of 10^{14} cm^{-3} and InAs of 10^{17} cm^{-3}, respectively. The red solid line and blue solid line with dots show opposite phases as the pump/probe pulses in parallel or antiparallel polarities, respectively; (c) InSb of 10^{14} and 10^{16} cm^{-3} at antiparallel case; (d) InAs of 10^{17} and 10^{16} cm^{-3} at antiparallel case; (e) and (f) show the spectra of the oscillatory features of InAs of 10^{17} and 10^{16} cm^{-3} in (d), respectively. The black arrows indicate the coherent vibration modes due to electron-phonon coupling

3.5 Overtones of two transverse acoustic phonons

To support the 2TA phonon modulations, several reasons are proposed to explain the observation. First, the dominant features at 2.2 THz (2TA) for InSb and 3.2 THz (2TA) for InAs, which are reported by previous publications [57–60], verify our observations for these two materials. Figure 23 shows 2TA Raman resonances of InSb, InAs, and InP compared with the overtones of two-phonon density of states calculated with an OVS model [60].

Second, the multi-phonon absorption in infrared spectrum occurs in both optical and acoustic phonons for polar or non-polar crystals. Compared with single-phonon

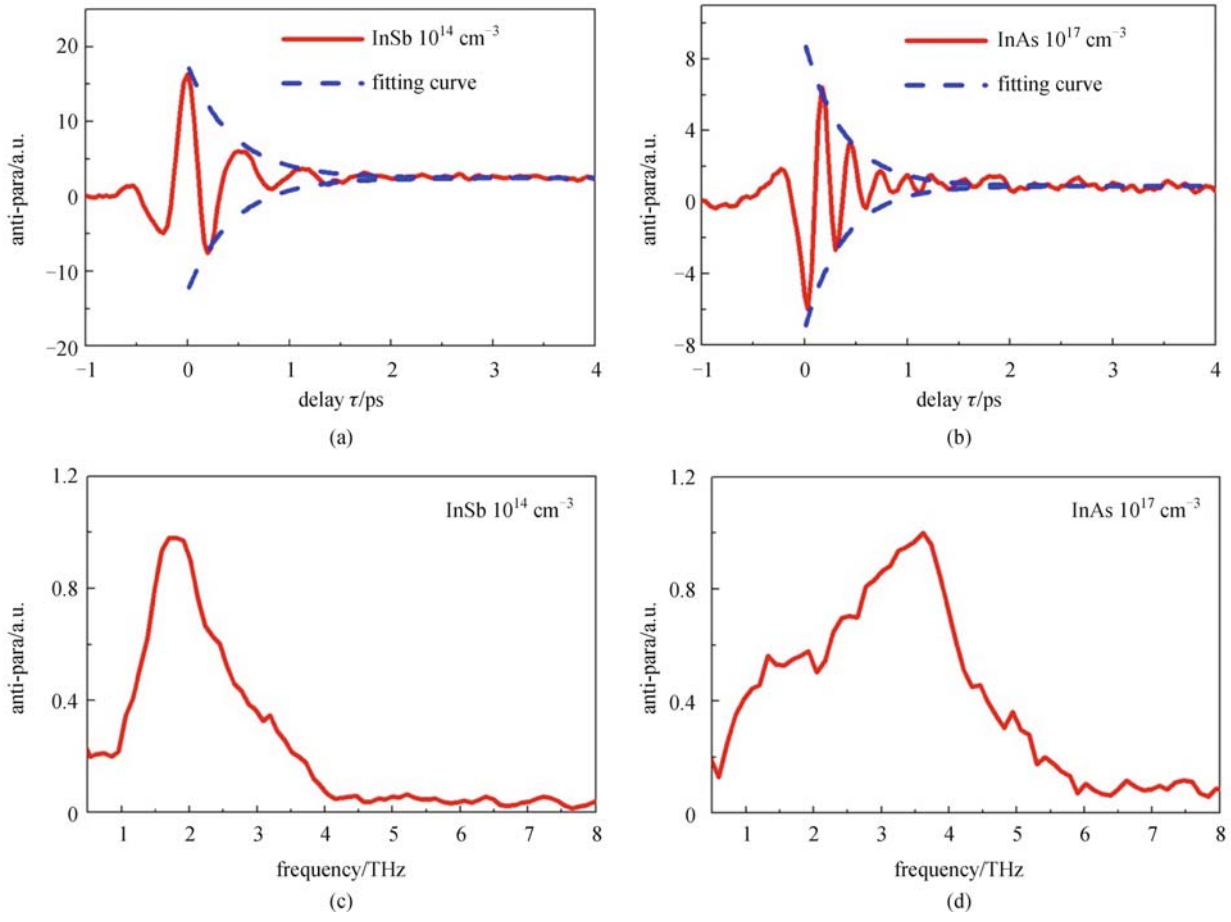

Fig. 22 (a) and (b) Waveforms retrieved by subtraction of the parallel and antiparallel cases in Figs. 21(a) and 21(b), respectively; (c) and (d) Fourier transforms of the retrieved waveforms in Figs. 22(a) and 22(b). The fitting curves are shown in blue dashed curves to estimate the coherent polaron damping time. Three point adjacent-averaging is applied

absorption, selection rules for multi-phonon absorption are more flexible. This is the reason why the 2TA phonon response could be monitored by far-infrared (THz) spectroscopy.

Third, the THz pump pulse drives the energetic electrons further to excite the 2TA phonon resonance. Concerning the deformation potential for InSb, the deformation potential of the 2TA phonon is one order smaller than that of the optical (TO) phonon [58]. Therefore, it is easier to perturb the 2TA phonon resonance than those of optical phonons.

Finally, the energy of the broadband THz pump pulse is close to the bandgaps of InSb and InAs, so that the multi-phonon responses are resonantly enhanced in these narrow bandgap semiconductors. This phenomenon is similar to resonance Raman spectroscopy where when the frequency of the laser beam is tuned to be near an electronic transition or material bandgap, Raman scattering intensity is greatly increased and multi-phonon absorption is easily observed [61]. As for the GaAs crystal with a carrier concentration of n-doped 10^{17} cm^{-3} measured in Fig. 24, whose bandgap is much larger than InSb and InAs, the coherent oscillation is not as obvious as the phenomena shown in the narrow bandgap semiconductors. Figure 24 shows the normalized reflection of the peak of THz probe field with pump/probe decay τ, where only a weak oscillatory feature shows around $\tau = 0$.

The coherent polaron damping time is estimated by fitting the oscillation features in Figs. 22(a) and 22(b) with an exponential decay function. Hence, the damping time is 0.45 ps for the InSb sample and 0.38 ps for the InAs sample.

3.6 Spectral response

A reflection measurement is performed with different THz field strengths to measure the InSb with a doping concentration of 10^{14} cm^{-3}. In contrast to the previous pump/probe approach which only measures the nonlinear response, the reflection measurement retrieves both linear and nonlinear responses of the sample. Figure 25(a) shows the reflections with THz fields at 15, 28 and 80 kV/cm. Instead of exhibiting a uniform reflection increase over the frequency range, a spectral peak around 2.2 THz is

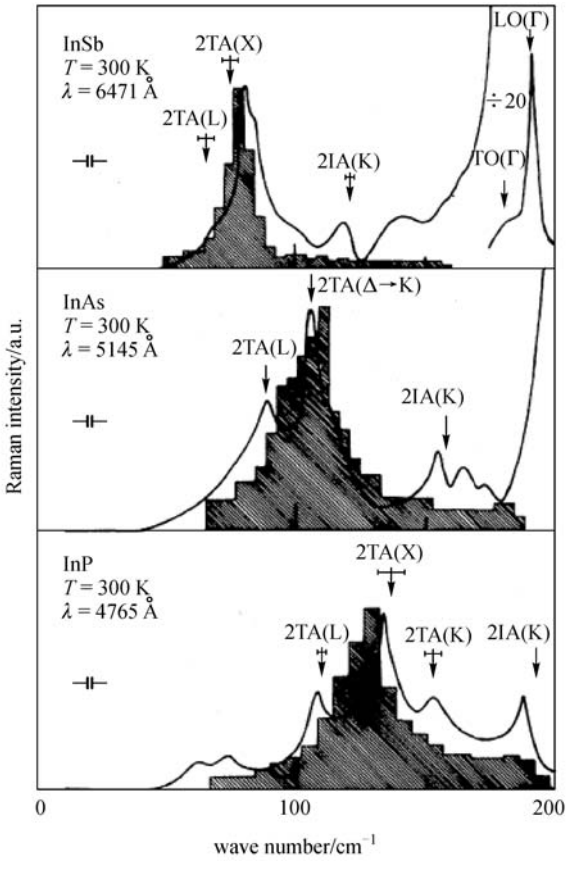

Fig. 23 Second-order acoustic Raman spectra of InSb, InAs, and InP compared with the overtones of two-phonon density of states calculated with the OVS model [59]

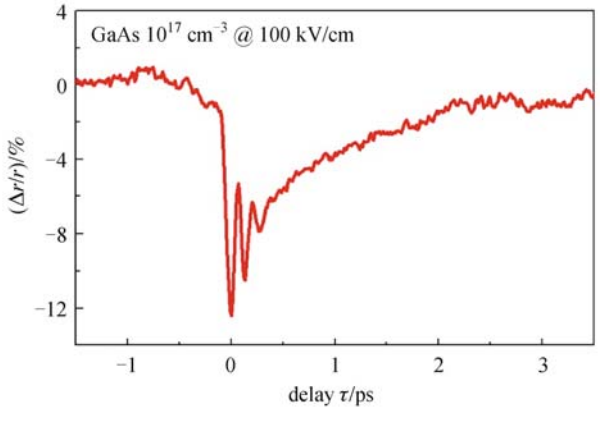

Fig. 24 n-doped GaAs at 100 kV/cm THz pump field and 15 kV/cm THz probe field

observed when the THz field strength is 80 kV/cm. It reproduces the 2TA phonon resonance and supports the 2 THz central frequency of the retrieved spectrum in Fig. 22 (c).

On the other hand, the TO phonon resonance is shown at 5.4 THz which agrees with previous infrared measurement [27]. Although the TO phonon resonance is clearly measured, it only shows small change with different field strengths, as shown in Fig. 25(a). In comparison to Figs. 21 and 22, if the optical phonon response is a pure linear effect, the differential method (pump/probe) will eliminate the linear contribution from the phonon response, and the nonlinear term related to the differential mobility remains. Furthermore, the nonlinear polaron oscillations can be time-resolved. However, in the reflection measurement, even though the nonlinear 2TA phonon response and the linear TO phonon resonance are both measurable, it only provides the spectral response but not transient carrier dynamics.

Figures 25(b) and 25(c) represent the refractive index and absorption coefficient of the InSb sample, respectively at 80 and 15 kV/cm field strengths. The data are retrieved from Fig. 25(a) based on solving Fresnel equations numerically [62], utilizing the fact that the THz pulse measurement contains phase information in addition to amplitude. According to the Drude-Lorentz model, the complex frequency-dependent dielectric function is

$$\varepsilon(\omega)=\varepsilon_{\infty}\left[1+\frac{\omega_{\mathrm{L}}^{2}-\omega_{\mathrm{T}}^{2}}{\omega_{\mathrm{T}}^{2}-\omega^{2}-\mathrm{i}\Gamma\omega}-\frac{\omega_{\mathrm{p}}^{2}}{\omega(\omega+\mathrm{i}\gamma)}\right], \qquad (10)$$

where $\varepsilon_{\infty}=15.68$, $\omega_{\mathrm{T}}=179.1$ cm^{-1}, $\omega_{\mathrm{L}}=190.4$ cm^{-1}, $\Gamma=4.6$ cm^{-1}, $\omega_{\mathrm{p}}=74.6$ cm^{-1}, and $\gamma=10.7$ cm^{-1} [27]. When the THz field is 15 kV/cm, the fitting curves (blue solid lines with dots in Figs. 25(b) and 25(c)) based on the Drude-Lorentz model are in a good agreement with the measurement results. However, when the THz field reaches 80 kV/cm, the effective refractive index and absorption coefficient deviate dramatically from the linear Drude-Lorentz behavior. A predominant real part of refractive index around 2.2 THz in Fig. 25(b) and an extruded absorption band from 2 to 5 THz in Fig. 25(c) verify the electron interacting with 2TA phonon modes [57–60] at a strong THz field (80 kV/cm).

3.7 Summary

The polaron nonlinear modulations are demonstrated in n-doped semiconductors on the sub-picosecond time scale. By utilizing an all-THz pump/probe scheme, the modulated reflections due to the excitations of acoustic modes are retrieved. With a single THz beam excitation onto the InSb sample, it exclusively highlights the electron-phonon interaction, which causes the increase of THz reflection around the overtones of 2TA phonon modes. The nonlinear modulation, performed with a reflective, room-temperature, and polarity-control spectrometer, provides a unique method for material identification, especially when linear features are suppressed.

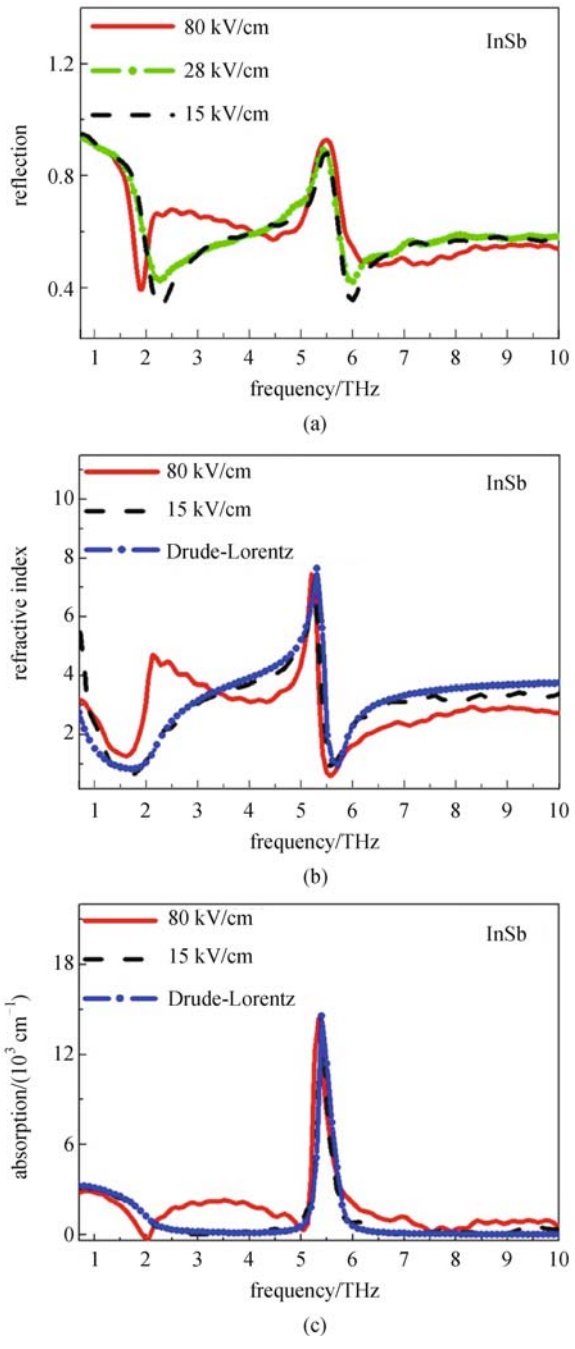

Fig. 25 Reflection measurement with THz-ABCD. (a) Reflections are of different THz field strengths in InSb of 10^{14} cm^{-3}; (b) and (c) refractive index (real part) and absorption coefficient according to (a)

4 Conclusions

This paper focuses on the underlying physics of semiconductor nonlinear dynamics and provides theoretical as well as experimental verifications. By a reflective geometry with a novel THz-ABCD technique, an ultra-broadband (0.5 – 35 THz) and time-resolved THz spectroscopy is utilized.

Section 1 shows a detailed design and performance of a R-THz-ABCD system, and demonstrates a system examination and comparison with FTIR as well as conventional THz-TDS. Compared to transitional THz-TDS, R-THz-ABCD has a remarkably broad bandwidth as well as at least one order larger peak THz field. Compared to FTIR, R-THz-ABCD provides time-resolved optical gating and several orders larger peak electric field. The THz-ABCD system is used as a platform for studying carrier dynamics in Sections 2 and 3 in order to investigate the semiconductor physics in the high field regime.

In Section 2, electron intervalley scattering and impact ionization of bulk InAs under high-field excitation are observed on a sub-picosecond time scale. It is shown that for p-doped InAs, the cascaded carrier generation dominates, while for n-doped InAs, both mechanisms have to be considered. With a single THz beam excitation on the n-doped InAs at different field strengths, the electron fractional occupation between the Γ and L valleys is experimentally estimated, which reflects the recently published work regarding Monte Carlo simulation of electron valley transfer.

Furthermore, in Section 3, a coherent polaron oscillation excited by intense THz pulses in n-doped semiconductors is investigated. Through modulations of reflection with a THz pump/probe technique, this work verifies the interaction between energetic electrons and a phonon field, and shows that this interaction applies for acoustic phonon modes. A novel method is proposed to diagnose the intrinsic properties of semiconductors with acoustic phonon responses, even though the acoustic phonon responses were difficult to monitor with past infrared measurement.

This paper provides a new vision of intense THz field interacting with semiconductors. The polaron modulation, for example, bridges the relationship between the infrared and Raman spectroscopy. Furthermore, the light-matter interaction of intense field is still promising and attractive for study in material nonlinearity. In particular, as the THz field strength reaches above 1 MV/cm, its magnetic component becomes considerable. A new study, so called Spintronics, to coherently control collective spin excitations in solids is a promising application in quantum optics, and the studies in this regime have just begun.

This paper has demonstrated nonlinear semiconductor dynamics based on a reflective geometry at room temperature. To extend the study by integrating a low temperature facility into the R-THz-ABCD spectrometer, more exciting phenomena, which only appear in low temperature, such as coherent exciton evolution and electron coupling in quantum structures will be achieved.

References

1. Cook D J, Hochstrasser R M. Intense terahertz pulses by four-wave rectification in air. Optics Letters, 2000, 25(16): 1210–1212
2. Xie X, Dai J, Zhang X C. Coherent control of THz wave generation in ambient air. Physical Review Letters, 2006, 96(7): 075005-1–075005-4
3. Kim K Y, Glownia J H, Taylor A J, Rodriguez G. Terahertz emission from ultrafast ionizing air in symmetry-broken laser fields. Optics Express, 2007, 15(8): 4577–4584
4. Karpowicz N, Zhang X C. Coherent terahertz echo of tunnel ionization in gases. Physical Review Letters, 2009, 102(9): 093001-1–093001-4
5. Dai J, Xie X, Zhang X C. Detection of broadband terahertz waves with a laser-induced plasma in gases. Physical Review Letters, 2006, 97(10): 103903-1–103903-4
6. Karpowicz N, Dai J M, Lu X, Chen Y, Yamaguchi M, Zhao H, Zhang X C, Zhang L, Zhang C, Price-Gallagher M, Fletcher C, Mamer O, Lesimple A, Johnson K. Coherent heterodyne time-domain spectrometry covering the entire "terahertz gap". Applied Physics Letters, 2008, 92(1): 011131-1–011131-3
7. Ho I C, Guo X, Zhang X C. Design and performance of reflective terahertz air-biased-coherent-detection for time-domain spectroscopy. Optics Express, 2010, 18(3): 2872–2883
8. Hu B B, Nuss M C. Imaging with terahertz waves. Optics Letters, 1995, 20(16): 1716–1718
9. Mittleman D M, Jacobsen R H, Nuss M C. T-ray imaging. IEEE Journal on Selected Topics in Quantum Electronics, 1996, 2(3): 679–692
10. Ferguson B, Zhang X C. Materials for terahertz science and technology. Nature Materials, 2002, 1(1): 26–33
11. Grischkowsky D, Keiding S, Exter M V, Fattinger Ch. Far-infrared time-domain spectroscopy with terahertz beams of dielectrics and semiconductors. Journal of the Optical Society of America B, Optical Physics, 1990, 7(10): 2006–2015
12. Nuss M C, Auston D H, Capasso F. Direct subpicosecond measurement of carrier mobility of photoexcited electrons in gallium arsenide. Physical Review Letters, 1987, 58(22): 2355–2358
13. Stepanov A G, Hebling J, Kuhl J. Efficient generation of subpicosecond terahertz radiation by phase-matched optical rectification using ultrashort laser pulses with tilted pulse fronts. Applied Physics Letters, 2003, 83(15): 3000–3002
14. Yeh K L, Hoffmann M C, Hebling J, Nelson K A. Generation of 10 μJ ultrashort terahertz pulses by optical rectification. Applied Physics Letters, 2007, 90(17): 171121
15. McLaughlin C V, Hayden L M, Polishak B, Huang S, Luo J, Kim T D, Jen A K Y. Wideband 15 THz response using organic electro-optic polymer emitter-sensor pairs at telecommunication wavelengths. Applied Physics Letters, 2008, 92(15): 151107-1–151107-3
16. Hamster H, Sullivan A, Gordon S, White W, Falcone R W. Subpicosecond, electromagnetic pulses from intense laser-plasma interaction. Physical Review Letters, 1993, 71(17): 2725–2728
17. Bartel T, Gaal P, Reimann K, Woerner M, Elsaesser T. Generation of single-cycle THz transients with high electric-field amplitudes. Optics Letters, 2005, 30(20): 2805–2807
18. Lu X, Karpowicz N, Zhang X C. Broadband terahertz detection with selected gases. Journal of the Optical Society of America B, Optical Physics, 2009, 26(9): A66–A73
19. Rønne C, Thrane L, Åstrand P O, Wallqvist A, Mikkelsen K V, Keiding S R. Investigation of the temperature dependence of dielectric relaxation in liquid water by THz reflection spectroscopy and molecular dynamics simulation. Journal of Chemical Physics, 1997, 107(14): 5319–5351
20. Hashimshony D, Geltner I, Cohen G, Avitzour Y, Zigler A, Smith C. Characterization of the electrical properties and thickness of thin epitaxial semiconductor layers by THz reflection spectroscopy. Journal of Applied Physics, 2001, 90(11): 5778–5781
21. Shon C H, Chong W Y, Jeon S G, Kim G J, Kim J I, Jin Y S. High speed terahertz pulse imaging in the reflection geometry and image quality enhancement by digital image processing. International Journal of Infrared and Millimeter Waves, 2008, 29(1): 79–88
22. Khazan M, Meissner R, Wilke I. Convertible transmission-reflection time-domain terahertz spectrometer. Review of Scientific Instruments, 2001, 72(8): 3427–3430
23. Pashkin A, Kempa M, Němec H, Kadlec F, Kužel P. Phase-sensitive time-domain terahertz reflection spectroscopy. Review of Scientific Instruments, 2003, 74(11): 4711–4717
24. Nashima S, Morikawa O, Takata K, Hangyo M. Measurement of optical properties of highly doped silicon by terahertz time domain reflection spectroscopy. Applied Physics Letters, 2001, 79(24): 3923–3925
25. Jeon T I, Grischkowsky D. Characterization of optically dense, doped semiconductors by reflection THz time domain spectroscopy. Applied Physics Letters, 1998, 72(23): 3032–3034
26. Watanabe S, Kondo R, Kagoshima S, Shimano R. Spin-density-wave gap in $(TMTSF)_2PF_6$ probed by reflection-type terahertz time-domain spectroscopy. Physica Status Solidi. B, Basic Research, 2008, 245(12): 2688–2691
27. Palik E D, ed. Silicon (Si), Calcium Carbonate, Calcite ($CaCO_3$), Indium Arsenide (InAs), and Indium Antimonide (InSb) in Handbook of Optical Constants of Solids. New York: Elsevier, 1998
28. Naftaly M, Dudley R. Methodologies for determining the dynamic ranges and signal-to-noise ratios of terahertz time-domain spectrometers. Optics Letters, 2009, 34(8): 1213–1215
29. Hase M, Kitajima M, Constantinescu A M, Petek H. The birth of a quasiparticle in silicon observed in time-frequency space. Nature, 2003, 426(6962): 51–54
30. Cheville R A, Grischkowsky D. Far-infrared terahertz time-domain spectroscopy of flames. Optics Letters, 1995, 20(15): 1646–1648
31. Podobedov V B, Plusquellic D F, Siegrist K E, Fraser G T, Ma Q, Tipping R H. New measurements of the water vapor continuum in the region from 0.3 to 2.7 THz. Journal of Quantitative Spectroscopy & Radiative Transfer, 2008, 109(3): 458–467
32. Liu J, Zhang X C. Birefringence and absorption coefficients of alpha barium borate in terahertz range. Journal of Applied Physics, 2009, 106(2): 023107-1–023107-5
33. Akturk S, Couairon A, Franco M, Mysyrowicz A. Spectrogram

representation of pulse self compression by filamentation. Optics Express, 2008, 16(22): 17626–17636
34. Bignell L J, Lewis R A. Reflectance studies of candidate THz emitters. Journal of Materials Science Materials in Electronics, 2009, 20(1): 326–331
35. Wu Q, Sun F G, Campbell P, Zhang X C. Dynamic range of an electro-optic field sensor and its imaging applications. Applied Physics Letters, 1996, 68(23): 3224–3326
36. Han P Y, Tani M, Usami M, Kono S, Kersting R, Zhang X C. A direct comparison between terahertz time-domain spectroscopy and far-infrared Fourier transform spectroscopy. Journal of Applied Physics, 2001, 89(4): 2357–2359
37. Sze S M, Ng K K. Physics of Semiconductor Devices. New Jersey: John Wiley & Sons, 2006
38. Dumke W P. Theory of avalanche breakdown in InSb and InAs. Physical Review, 1968, 167(3): 783–789
39. Rode D L. Electron transport in InSb, InAs, and InP. Physical Review B: Condensed Matter and Materials Physics, 1971, 3(10): 3287–3299
40. Brennan K, Hess K. High field transport in GaAs, InP and InAs. Solid-State Electronics, 1984, 27(4): 347–357
41. Brennan K F, Mansour N S. Monte Carlo calculation of electron impact ionization in bulk InAs and HgCdTe. Journal of Applied Physics, 1991, 69(11): 7844–7847
42. Ganichev S D, Diener J, Yassievich I N, Prettl W. Poole-Frenkel effect in terahertz electromagnetic fields. Europhysics Letters, 1995, 29(4): 315–320
43. Markelz A G, Asmar N G, Brar B, Gwinn E G. Interband impact ionization by terahertz illumination of InAs heterostructures. Applied Physics Letters, 1996, 69(26): 3975–3977
44. Devreese J T, van Welzenis R G. Impact ionisation probability in InSb. Applied Physics A, Solids and Surfaces, 1982, 29(3): 125–132
45. Su F H, Blanchard F, Sharma G, Razzari L, Ayesheshim A, Cocker T L, Titova L V, Ozaki T, Kieffer J C, Morandotti R, Reid M, Hegmann F A. Terahertz pulse induced intervalley scattering in photoexcited GaAs. Optics Express, 2009, 17(12): 9620–9629
46. Hoffmann M C, Hebling J, Hwang H Y, Yeh K L, Nelson K A. Impact ionization in InSb probed by terahertz pump—terahertz probe spectroscopy. Physical Review B: Condensed Matter and Materials Physics, 2009, 79(16): 161201-1–161201-4
47. Razzari L, Su F H, Sharma G, Blanchard F, Ayesheshim A, Bandulet H C, Morandotti R, Kieffer J C, Ozaki T, Reid M, Hegmann F A. Nonlinear ultrafast modulation of the optical absorption of intense few-cycle terahertz pulses in n-doped semiconductors. Physical Review B: Condensed Matter and Materials Physics, 2009, 79(19): 193204-1–193204-4
48. Wen H, Wiczer M, Lindenberg A M. Ultrafast electron cascades in semiconductors driven by intense femtosecond terahertz pulses. Physical Review B: Condensed Matter and Materials Physics, 2008, 78(12): 125203
49. Arabshahi H, Golafrooz S. Monte Carlo based calculation of electron transport properties in bulk InAs, AlAs and InAlAs. Bulgarian Journal of Physics, 2010, 37(4): 215–222
50. Fröhlich H. Electrons in lattice fields. Advances in Physics, 1954, 3 (11): 325–361
51. Kuehn W, Gaal P, Reimann K, Woerner M, Elsaesser T, Hey R. Coherent ballistic motion of electrons in a periodic potential. Physical Review Letters, 2010, 104(14): 146602
52. Kuehn W, Gaal P, Reimann K, Woerner M, Elsaesser T, Hey R. Terahertz-induced interband tunneling of electrons in GaAs. Physical Review B: Condensed Matter and Materials Physics, 2010, 82(7): 075204-1–075204-8
53. Gaal P, Kuehn W, Reimann K, Woerner M, Elsaesser T, Hey R. Internal motions of a quasiparticle governing its ultrafast nonlinear response. Nature, 2007, 450(7173): 1210–1213
54. Meinert G, Bányai L, Gartner P. Classical polarons in a constant electric field. Physical Review B: Condensed Matter and Materials Physics, 2001, 63(24): 245203-1–245203-8
55. Bányai L. Motion of a classical polaron in a dc electric field. Physical Review Letters, 1993, 70(11): 1674–1677
56. Ho I C, Zhang X C. Driving intervalley scattering and impact ionization in InAs with intense terahertz pulses. Applied Physics Letters, 2011, 98(24): 241908-1–241908-3
57. Koteles E S, Datars W R, Dolling G. Far-infrared phonon absorption in InSb. Physical Review B: Condensed Matter and Materials Physics, 1974, 9(2): 572–582
58. Kiefer W, Richter W, Cardona M. Second-order Raman scattering in InSb. Physical Review B: Condensed Matter and Materials Physics, 1975, 12(6): 2346–2354
59. Carles R, Saint-Cricq N, Renucci J B, Renucci M A, Zwick A. Second-order Raman scattering in InAs. Physical Review B: Condensed Matter and Materials Physics, 1980, 22(10): 4804–4815
60. Borcherds P H, Kunc K. The lattice dynamics of indium pnictides. Journal of Physical Chemistry, 1978, 11(20): 4145–4155
61. Smith E, Dent G. Modern Raman Spectroscopy. West Sussex: John Wiley & Sons, 2005
62. Hecht E. Optics. San Francisco: Addison Wesley, 2002

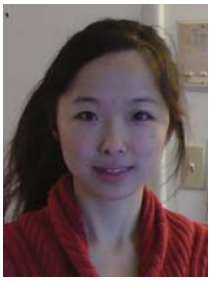

I-Chen Ho received the B.S. degree in physics from Taiwan Normal University, Taipei, Taiwan, in 2004, and the M.S. degree in photonics from Chiao Tung University, Hsinchu, Taiwan, in 2007. She received the Ph.D. degree in physics from Rensselaer Polytechnic Institute, Troy, NY, in 2011. She was engaged in design of ultra-broadband terahertz spectroscopy and dedicated her research to high-field, transient carrier dynamics in semiconductors.

She currently is an Engineer in Intel Corporation, Hillsboro, Oregon. She is the author or coauthor of more than 10 refereed journal papers as well as contribution to book chapters and has delivered over 10 conference presentations.

Dr. Ho was awarded the Coherent Graduate Student Award from Coherent Inc. in 2010, the Founders Award of Excellence at Rensselaer in 2008, the President Award at Chiao Tung University in 2006, the President Award at Taiwan Normal University in 2004, and the Excellent Student Award at Taiwan Normal University in 2003.

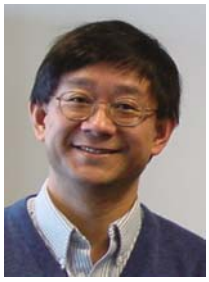

Xi-Cheng Zhang–Parker Givens Chair of Optics, assumes Directorship of The Institute of Optics, University of Rochester (UR), NY, a foremost institution in optics and optical physics research and education, on 1/1/2012. Prior to joining UR, he pioneered world-leading research in the field of ultrafast laser-based terahertz technology and optical physics at Rensselaer Polytechnic Institute (RPI), Troy NY (1992 − 2012). At RPI, he is the Eric Jonsson Professor of Science; Acting Head at the Department of Physics, Applied Physics & Astronomy; Professor of Electrical, Computer & System; and Founding Director of the Center for THz Research. He is co-founder of Zomega Terahertz Corp. With a B.S. (1982) from Peking University, he earned the M.S. (1983) and Ph.D. degree (1985) in Physics from Brown University, RI.

Previous positions included Visiting Scientist at MIT (1985), Physical Tech. Division of Amoco Research Center (1987), EE Dept. at Columbia University (1987–1991); Distinguished Visiting Scientist at Jet Propulsion Lab, Caltech (2006). He holds 27 U.S. patents, and is a prolific author and speaker. He is a Fellow of AAAS, APS (lifetime), IEEE, OSA (lifetime), and SPIE (lifetime). Dr. Zhang is serving as Editor-in-Chief of Optics Letters (2014 − 2016).

His honors and awards include: IRMMW-THz Kenneth Button Prize (2014); OSA William F. Meggers Award (2012); IEEE Photonics Society William Streifer Scientific Achievement Award (2011); Rensselaer William H. Wiley 1866 Award (2009); Japan Society for the Promotion of Science Fellowship & NRC-CIAR Distinguished Visiting Scientist, Ottawa, Canada (2004); and First Heinrich Rudolf Hertz Lecturer, RWTH, Aachen, Germany (2003). He also served two years as a Distinguished Lecturer of IEEE/LEOS. He received Rensselaer Early Career Award (1996), Research Corporation Cottrell Scholar Award (1995), NSF Early Career Award (1995), K.C. Wong Prize, K.C. Wong Foundation, Hong Kong (1995), NSF Research Initiation Award (1992). In 1993 − 1994, he was an AFOSR-SRPF Fellow at Hanscom Air Force Base.